Structure Formation and Surface Chemistry of Ionic Liquids on Model Electrode Surfaces – Model Studies for the Electrode | Electrolyte Interface in Li-ion Batteries

Florian Buchner,[‡,a,b,c] *Benedikt Uhl,*[‡,c] *Katrin Forster-Tonigold,*[‡,a,b] *Joachim Bansmann,*[c] *Axel Groß,*[a,d] *and R. Jürgen Behm,**[a,c]

[a] Helmholtz Institute Ulm Electrochemical Energy Storage (HIU), Helmholtzstraße 11, D–89081 Ulm, Germany

[b] Karlsruhe Institute of Technology (KIT), P.O. Box 3640, 76021 Karlsruhe, Germany

[c] Ulm University, Institute of Surface Chemistry and Catalysis, Albert-Einstein-Allee 47, D–89081 Ulm, Germany

[d] Ulm University, Institute of Theoretical Chemistry, Albert-Einstein-Allee 11, D–89081 Ulm, Germany

Prof. Dr. R. J. Behm
Universität Ulm
Institut für Oberflächenchemie und Katalyse
Albert–Einstein–Allee 47
D–89069 Ulm, Germany
Phone: +49 (0)731/50–25451
Fax: +49 (0)731/50–25452
E–Mail: juergen.behm@uni–ulm.de

‡ These authors contributed equally

ABSTRACT

Ionic liquids (ILs) are considered as attractive electrolyte solvents in modern battery concepts such as Li-ion batteries. Here we present a comprehensive review of results of previous model studies on the interaction of the battery relevant IL 1-butyl-1-methylpyrrolidinium bis(trifluoromethylsulfonyl)imide ($[BMP]^+[TFSI]^-$) with a series of structurally and chemically well-defined model electrode surfaces, which are increasingly complex and relevant for battery applications (Ag(111), Au(111), Cu(111), pristine and lithiated HOPG, rutile TiO_2(110)). Combining surface science techniques such as high resolution scanning tunneling microscopy (STM) and X-ray photoelectron spectroscopy (XPS) for characterizing surface structure and chemical composition in deposited (sub-)monolayer adlayers with dispersion corrected density functional theory (DFT-D) based calculations, this work aims at a molecular scale understanding of the fundamental processes at the electrode|electrolyte interface, which are crucial for the development of the so-called solid electrolyte interphase (SEI) layer in batteries. Performed under idealized conditions, in an ultrahigh vacuum (UHV) environment, these model studies provide detailed insights on the structure formation in the adlayer, the substrate - adsorbate and adsorbate – adsorbate interactions responsible for this, and the tendency for chemically induced decomposition of the IL. To mimic the situation in an electrolyte, we also investigated the interaction of adsorbed IL (sub-)monolayers with coadsorbed lithium. Even at 80 K, postdeposited Li is found to react with the IL, leading to decomposition products such as LiF, Li_3N, Li_2S, Li_xSO_y, Li_2O etc.. In the absence of a $[BMP]^+[TFSI]^-$ adlayer, it tends to adsorb, dissolve or intercalate into the substrate (metals, HOPG) or to react with the substrate (TiO_2) above a critical temperature, forming LiO_x and Ti^{3+} species in the latter case. Finally, the formation of stable decomposition products was found to sensitively change the equilibrium between surface Li and Li^+ intercalated in the bulk, leading to a deintercalation from lithiated HOPG in the presence of an adsorbed IL adlayer at > 230 K. Overall, these results provide detailed insights into the surface chemistry at the solid|electrolyte interface and the initial stages of SEI formation at electrode surfaces in the absence of an applied potential, which is essential for the further improvement of future Li-ion batteries.

I. INTRODUCTION

Ionic liquids (ILs), which are defined as molten salts with a melting point below 100°C that largely consist of organic ions,[1,2] have attracted much attention in science and technology recently.[3-10] Due to their high ionic conductivity, electrochemical stability and low flammability, they are highly promising candidates for application as solvent in battery electrolytes, e.g., for efficient and safe Li-ion and Li-air batteries.[11-14] Most important and often decisive for the stable operation of Li-ion batteries is the formation of the so-called solid|electrolyte interphase (SEI), an interfacial layer at the electrode|electrolyte interface,[15-19] which is formed by the decomposition of electrolyte during the first charging / discharging cycle. This layer serves as Li^+ ion conductor and, at the same time, as electron insulator.

Aiming at a molecular scale understanding of the interactions between electrodes and electrolytes in Li-ion batteries, we have systematically investigated the interface structure and structure formation at different IL|solid interfaces, employing different surface science techniques. We first investigated the interaction of individual components of the electrolytes (solvent, shuttle ion), with structurally and chemically well-defined model electrode surfaces under idealized conditions in an ultrahigh vacuum (UHV) environment, focusing on the structure formation and surface chemistry.[20-30] The measurements were performed in the absence of an applied potential between electrode and electrolyte, which is equivalent to the situation under open circuit conditions, employing methods that are sensitive to the adsorbate structure and to the surface chemistry on planar model surfaces such as high resolution scanning tunneling microscopy (STM) and X-ray photoelectron spectroscopy (XPS). The experimental work was complemented by dispersion corrected density functional theory (DFT-D) based calculations. Starting with close-packed coinage metal surfaces such as Ag(111),[20,22] Au(111)[21,22,25] and Cu(111),[23,24] we then moved to more realistic model surfaces such as pristine highly oriented pyrolytic graphite (HOPG)[26,27] and rutile TiO_2(110),[28] which

are both Li-intercalation anode materials in Li-ion batteries.[16,31] In addition, to mimic the chemical SEI formation at different IL|solid interfaces, we studied the interaction of Li with Cu(111)[24], TiO_2(110)[28] and HOPG[27] surfaces and of IL adlayers with Li, which was either postdeposited by vapor deposition of Li from the gas phase or, in the case of lithiated graphite, available as Li^+ in the bulk. This approach is considered to provide detailed information on the surface chemistry in the initial stages of the solid|electrolyte interphase formation at the electrode|electrolyte interface, which is urgently needed for the systematic improvement of tailored SEIs for future Li-ion batteries.

In the present article, we put our previous results on the structure formation and surface chemistry of adsorbed IL (sub-)monolayers into a common perspective. We will concentrate on adsorption and reaction studies using the battery-relevant IL butyl-1-methylpyrrolidinium bis(trifluoromethylsulfonyl)imide $[BMP]^+[TFSI]^-$. It should be noted that a number of different abbreviations such as $[BMP]^+[TFSI]^-$,[27] $[BMP]^+[TFSA]^-$,[32,33] $[Py_{1,4}]$TFSA,[34] $[Py_{1,4}]$TFSI[35] and $[C_4C_1Pyrr]^+[Tf_2N]^-$[36,37] have been used for this compound previously.

Before starting with the selective review, we will briefly summarize the most important results relevant for this work which had been reported previously. The interaction of a few $[TFSI]^-$-based ILs with different cations with single crystalline surfaces has been investigated (*ex situ*) under UHV conditions[35-49] and *in-situ* in an electrochemical environment.[32-34,50-55] For example, employing angle-resolved X-ray photoelectron spectroscopy (ARXPS), Cremer *et al.* had concluded that in the first layer the ILs 1,3-dimethylimidazolium bis(trifluoromethylsulfonyl)imide ($[MMIM]^+[TFSA]^-$) and 1-methyl-3-octylimidazolium bis(trifluoromethylsulfonyl)imide ($[OMIM]^+$ $[TFSA]^-$) adsorb presumably in an alternating ("checkerboard") arrangement on Au(111), with both anions and cations bound directly to the surface. The octyl group of $[OMIM]^+$ was concluded to be parallel to the surface; for higher coverage the octyl group most likely changes its orientation and points upwards, away from

the surface.[40] Foulston *et al.*[39] resolved molecular features in a 1-methyl-3-ethylimidazolium bis(trifluoromethylsulfonyl)imide ($[EMIM]^+[TFSA]^-$) adlayer adsorbed on Au(110) in UHV STM measurements. They could not, however, distinguish between anions and cations. In an *in situ* STM study, Carstens et al.[52] resolved different molecular patterns at cathodic potentials of ~ –2 V at the $[OMIM]^+$ $[TFSA]^-$|HOPG interface, which they associated with adsorbed cations. Investigating the interaction of $[EMIM]^+[TFSA]^-$ with the basal plane of HOPG by *in situ* AFM, Elbourne et al.[53] resolved a height-modulated row-like structure at open circuit potential and changes in these rows upon varying the potential by *in situ* atomic force microscopy (AFM) measurements. Finally, Wen et. al.[33] identified potential dependent structures at the $[BMP]^+[TFSI]^-$|Au(111) interface by *in situ* STM measurements. They found that the unit cell size decreases with potential from -1.4 to -1.6 V, which they assigned to conformational changes of the $[BMP]^+$ cations. From the above AFM/STM measurements, it was possible to indirectly conclude on the presence of anions or cations, based on the structural changes at different applied potentials. It was not possible in these studies, however, to reach (sub-)molecular resolution, which would directly allow identifying anions and cations at IL|solid interfaces. In total, despite of these insights, a better understanding of these interfaces is highly desirable, including the clear identification of adsorbed anions and cations, the understanding of the nature of substrate – adsorbate and adsorbate – adsorbate interactions, and finally a better understanding of the surface chemistry at the interface.

Considering the interaction of Li with ILs, Aurbach et al. suggested based on electrochemical measurements that the reduction of $[TFSI]^-$ results in products of $[Li]^+[TFSI]^-$ such as Li_3N, $Li_2S_2O_4$, LiF, $C_2F_xLi_y$, $Li_2NSO_2CF_3$, $LiSO_2CF_3$, $Li_2S_2O_4$, Li_2S, Li_2O and Li_2SO_3.[56] In a computational study, using ab initio molecular dynamic simulations with electric fields, Ando et al. predicted that $[TFSI]^-$ is reduced on lithium independent of the applied potential, resulting in the formation of LiF.[57] Despite of these results, however,

the fundamental understanding of the interaction of ILs and Li adsorbed on single crystalline electrode surfaces is rare.

In the following, we will first compare the adlayer structures formed upon deposition of (sub-)monolayer amounts of $[BMP]^+[TFSI]^-$ on the different substrates, going from inert noble metal and HOPG to more reactive surfaces (Cu(111), rutile TiO_2(110)) (section A). In the next section we will evaluate and compare the thermal stability of the IL in contact with the different model electrodes, and map out trends for decomposition (section B). Third, we will discuss the influence of coadsorbed Li on the adsorption and decomposition of $[BMP]^+[TFSI]^-$ on selected model electrode surfaces (HOPG, Cu(111), TiO_2(110)), exploring first the interaction of Li with the pristine surfaces, which provides information on the adsorption, dissolution and (de-)intercalation behavior of Li, and then the interaction of postdeposited Li on (sub-)monolayers of the preadsorbed IL (section C). Finally the main trends that can be derived from these data will be discussed (section D).

II. METHODS

A. Experiment

The experiments were carried out in a commercial UHV system (SPECS) with a base pressure of 2×10^{-10} mbar. It consists of two chambers, one containing an Aarhus-type STM/AFM system (SPECS Aarhus SPM150 with Colibri sensor), the other one is equipped with an X-ray source (SPECS XR50, Al-K_α and Mg-K_α), a He lamp (SPECS UVS 300) and a hemispherical analyzer (SPECS, DLSEGD-Phoibos-Has3500) for XPS and UPS measurements.

The Cu(111), Ag(111), HOPG and TiO_2(110) samples were purchased from MaTecK. The Ag(111), Cu(111) and TiO_2(110) samples have a hat-shaped form with a diameter of 9 mm, one side is polished with a roughness smaller than 30 nm and an orientation accuracy of

< 0.1°. Clean Ag(111) surfaces were prepared by Ar^+-ion sputtering (500 eV) and annealing to 770 K. The Cu(111) surface was cleaned by Ar^+ ion sputtering (1 kV) and heating to 820 K with the manipulator head simultaneously being cooled by liquid N_2 (for details cf. ref.[24]). The highly oriented pyrolytic graphite(0001) (HOPG) (ZYA, mosaic spread 0.4°± 0.1° / cuboid shape with a size of 5 mm × 5 mm × < 0.5 mm for the STM measurements and 10 mm × 10 mm × < 1 mm for XPS), was annealed at ~ 900 K for 1 h in UHV to generate a clean graphite(0001) surface. Rutile TiO_2(110) crystals were first calcined at 1173 K under air atmosphere and then transferred into the UHV chamber and annealed in UHV to 1023 K for 5 h, which partially reduces the sample, to generate a sufficient conductivity for the STM measurements. To achieve a properly prepared smooth (110) surface, several cycles of Ar^+ ion sputtering (0.5 kV, 45 min) and heating to 973 K for 30 min were carried out (for details about the initial cleaning procedure cf. ref.[28,58]).

The ionic liquid $[BMP]^+[TFSI]^-$ was purchased from Merck in ultrapure quality. The ionic liquid was filled into a quartz crucible, which was mounted in a Knudsen effusion cell (Ventiotec, OVD-3). To generate IL adlayers, we evaporated the IL at a temperature of the IL source of 450 K. Under these conditions the deposition rate was ~ 0.1 ML min^{-1}, with 1 monolayer (ML) defined as a layer at saturation coverage.

Lithium metal dosing was carried out with an alkali getter source (SAES Getters). Exposures were made by resistively heating the source (7.1 A, 1.1 V) in line-of-sight of the samples at a distance of around 6 cm. Deposition rates of approximately 0.04 – 0.05 ML min^{-1} were calculated from the damping of the substrate peaks (C 1s, Cu 2p, Ti 2p) after successive vapor deposition of Li at temperatures where Li adsorbs on the surface. For the evaluation we assume that a ML has a thickness d of 2.48 Å, equivalent to the (110) interplanar distance in a body centered cubic crystal (the most stable configuration of a Li metal at r.t.). The layer thickness d was calculated by $I_d = I_0 \exp(-d / \lambda \cos\theta)$, with an electron inelastic mean free

path (IMFP) λ for electrons with kinetic energies of ~ 1200 eV (C 1s) in Li of 46 Å[59], for kinetic energies of ~ 554 eV (Cu 2p) in Li of 25 Å[59] and for kinetic energies of ~ 1027 eV (Ti 2p) in Li of 41 Å.[59]

For the work function measurements by UPS (He I: hν = 21.2 eV) at normal emission (0° to the surface normal), a bias voltage of –5.0 V was applied to the sample to accelerate the photoelectrons into the analyzer (pass energy, E_{pass} = 1 eV), which allows us to observe a clear electron cut-off ($E_{cut\text{-}off}$). The work function Φ was calculated by $\Phi = h\nu - E_{cut\text{-}off}$. For the XPS measurements we used an Al-K_α X-ray source (1486.6 eV), operated at a power of 250 W (U = 14 kV, I = 17.8 mA) on Cu and HOPG and with 150 W (U = 12 kV, I = 12.5 mA) on TiO_2(110). XP spectra were recorded at a pass energy E_{pass} of 100 eV at grazing emission (80° to the surface normal). For the fitting of the XP spectra we either subtracted the background before peak deconvolution or used a simultaneous fit of background (Shirley + slope) and signal, applying an asymmetric pseudo-Voigt-type function.

STM measurements were performed in constant current mode with currents between around 10 and 50 pA and bias voltages up to -2 V applied at the sample.

B. Theory

Periodic density functional theory calculations were performed using the exchange-correlation functional RPBE[60] and semi-empirical corrections for dispersion effects (DFT-D3)[61] in connection with a damping function proposed by Chai and Head-Gordon ("zerodamping")[62] as implemented in the Vienna ab initio simulation package (VASP 5.3.5).[63,64] This approach was shown to accurately reproduce properties related to liquid water[65,66] and the water-metal interaction.[67] Ion cores are represented by means of the projector-augmented wave (PAW) method.[68,69] The electronic one-particle wave functions were expanded in a plane-wave basis set up to an energy cutoff of 400 eV.

The Ag(111) and the graphite(0001) surfaces were represented by slabs consisting of 3 atomic layers, separated by a vacuum region of about 23-25 Å. The adsorption of quasi-isolated cation-anion pairs was modelled by a (5x5) overlayer structure on Ag(111) and a (6x6) overlayer structure on graphite(0001) each with one adsorbed IL pair per unit cell. For the integration over the first Brillouin zone we used a 2x2x1 Monkhorst-Pack k-point mesh[70] with a Methfessel-Paxton smearing of 0.1 eV (for Ag) and a Gaussian smearing of 0.05 eV (for graphite). The geometry of the adsorption complex was optimized by relaxing all atoms of the IL pair and the atoms of the uppermost layer of the surface. Furthermore, in case of Ag, only these atoms were taken into account for the evaluation of dispersive interactions in order to mimic the screening effect of the metal.[71]

To describe the adsorption on graphite(0001), a rectangular unit cell with the dimensions (8.58 Å × 14.86 Å) that reflects the periodicity observed in STM experiments was used in the calculations as well.[26] In these calculations the integration over the first Brillouin zone was adjusted by using a 5x3x1 Monkhorst-Pack k-point mesh.

The adsorption energy (E_{ad}) was calculated as E_{ad} = E(adsorption complex) - E(surface)-E(IL), where E(adsorption complex) denotes the energy of the optimized adsorption complex, E(surface) is the energy of the bare, optimized surface and E(IL) is the energy of an optimized $[BMP]^+[TFSI]^-$ pair in a large box. Information about contributions stemming from adsorbate-adsorbate and substrate-adsorbate interactions have been obtained as described in a previous publication[26].

STM simulations are based on the Tersoff-Hamann approximation.[72] Within that model the tunneling current is proportional to the local density of states (LDOS) close to the Fermi energy of the surface at the position of the center of the tip. Constant-current images are simulated by an isosurface of the LDOS integrated between the Fermi energy of the system and the sample bias (here: -1.35 eV for the adsorption of $[BMP]^+[TFSI]^-$ on Ag(111) and -

0.78 eV for the adsorption of $[BMP]^+[TFSI]^-$ on graphite(0001)). The values of the isosurfaces taken here are 3×10^{-7} eÅ^{-3} for the adsorption of $[BMP]^+[TFSI]^-$ on Ag(111) and 5×10^{-7} eÅ^{-3} for the adsorption of $[BMP]^+[TFSI]^-$ on graphite(0001). Note, for historical reasons STM images of $[BMP]^+[TFSI]^-$ on Ag(111) have been calculated using PBE-D3 instead of RPBE-D3 that has been used for all other calculations. Both DFT-functionals with semiempirical corrections for dispersion effects lead to very similar results regarding the adsorption geometry and the total adsorption energy. Due to the close relation of PBE and RPBE the charge density is expected to be comparable as well.

III. RESULTS AND DISCUSSION

A. Structure formation of $[BMP]^+[TFSI]^-$ (sub-)monolayers at low temperatures

To begin with, we compare the structure formation of $[BMP]^+[TFSI]^-$ (sub-)monolayers on several hexagonal closed packed surfaces such as Ag(111), Au(111), Cu(111) and HOPG and in addition on rutile TiO_2(110), based on large-scale STM images (Figure 1) and molecular resolution STM images (Figure 2) recorded at low-temperature. $[BMP]^+[TFSI]^-$ (sub-)monolayers were vapor deposited on the samples held at r.t. and subsequently cooled to ~ 100 K before STM imaging. The only exception was the reactive Cu(111) surface, where $[BMP]^+[TFSI]^-$ was adsorbed at ~ 200 K to avoid IL decomposition. Elevated adsorption temperatures were chosen to make sure that the formation of well-ordered arrangements is not kinetically hindered. It should be noted that for Ag(111), Au(111) and HOPG(0001) $[BMP]^+[TFSI]^-$ adsorbs reversibly in intact ion pairs.

1. $[BMP]^+[TFSI]^-$ |Ag(111)

After vapor deposition of a $[BMP]^+[TFSI]^-$ (sub-)monolayer on Ag(111) at r.t. the STM images revealed flat terraces with significant noise in the image (not shown), which is indicative for mobile molecular species that diffuse too fast below the STM tip to be resolved

on the timescale of the experiment, forming a two-dimensional (2D) gas / liquid phase.[20,22,23] Therefore, to reduce the mobility of the adspecies, the Ag(111) sample was cooled to ~ 100 K before the STM measurements.

The STM image in Figure 1a shows three silver terraces. On the upper two terraces no adsorbates are visible; the lower one is filled by a large, long-range ordered 2D crystalline phase with no internal domain boundaries. As described in more detail in ref.,[20] such 2D crystalline phases of $[BMP]^+[TFSI]^-$ usually cover large parts of the silver terraces; except on narrow terraces and in a few cases on larger terraces close to the steps. In these latter cases we observed areas with a short-range order in the IL adlayer, which was referred to as a 2D glass phase.[20] The 2D crystalline phases have been observed with different rotational orientations on different Ag(111) terraces in the same STM image, rotated by 120° or multiplies thereof, but only one orientation per terrace. The appearance of only 3 rotational domains reveals that the adlayer is aligned along the close-packed high symmetry directions of the (111) surface. Furthermore, the formation of highly ordered 2D crystalline phases is indicative for non-negligible interactions between adsorbed molecular moieties. On the other hand, the facts that even at 100 K the long-range ordered 2D crystalline phase is in equilibrium with a mobile 2D gas / liquid phase (molecules with high mobility), and that the 2D crystalline phase exhibits a low melting point of ~ 180 K point to rather weak attractive adsorbate – adsorbate interactions and a low barrier for surface diffusion.[20]

The high resolution STM images of the 2D crystalline phase on Ag(111) in Figure 2a resolve an alternating sequence of pairs of longish protrusions and dots (depicted by symbols). The dots are aligned in two directions (depicted by dashed lines) along the lattice vectors of the unit cell. The dimensions of the adlayer unit cell are $|\vec{A}| = 2.35 \pm 0.1$ nm, $|\vec{B}| = 1.15 \pm 0.1$ nm and $\alpha = 98 \pm 5°$, which approximately corresponds to a commensurate, rectangular $\begin{bmatrix} 10 & 4 \\ 0 & 4 \end{bmatrix}$

unit cell. The unit cell includes two of these dots and four longish protrusions. As illustrated in more detail in ref.[20], one dot and one pair of longish features represent one anion-cation pair, meaning that the unit cell includes two anion-cation pairs. The dot is related to the alkyl chain of the cation, which is pointing upward, away from the surface, and the two longish features represent the two CF_3 groups of each anion, also pointing upward. Further details about adsorbate-substrate interactions will be discussed together with the DFT-D calculations in Figure 4. The pairs of longish protrusions as well as the dots are arranged along the direction of one of the lattice vectors, respectively, where a line of dots is followed by line of longish protrusions and vice versa. The orientation of the longish protrusion is changed by ~ 120° in neighboring rows. Also these details point to a decisive influence of the atomic lattice of the Ag(111) surface structure on the adlayer structure. This is discussed in more detail in refs.[20,22].

2. $[BMP]^+[TFSI]^-$ | Au(111)

Adsorption of $[BMP]^+[TFSI]^-$ on the herringbone reconstructed Au(111) surface[73] leads to somewhat different structures at ~ 100 K compared to those formed on Ag(111) (Figure 1b). At monolayer coverage three different rotational domains of the 2D crystalline phases are observed. Since the underlying herringbone reconstruction pattern can still be resolved, we can also determine the relative orientation of the adlayer with respect to the reconstruction pattern (see below), and thus to the atomic lattice of the Au(111) surface. Obviously, also for this surface the Au(111) surface lattice has a decisive influence on the adlayer orientation with respect to the substrate, indicating that there are preferred adsorption geometries / sites and that the interaction between substrate and adlayer is significantly corrugated along the surface.

In contrast to Ag(111), where the size of the 2D crystalline domains is only limited by the steps, the 2D adlayer structure is additionally disturbed by the periodic changes in the

direction of the dislocation lines in the herringbone pattern by 120°. Obviously, the $[BMP]^+[TFSI]^-$ 2D crystalline phase on Au(111) is severely influenced by the herringbone reconstruction pattern, The resulting adlayer domains are separated by stripes with a short-range ordered 2D glass phase in between.

In addition, on Au(111) we also observed smaller islands / domains of the 2D crystalline phase at (sub-)monolayer coverage (cf. ref.[21,22]), different from Ag(111). Apparently, the herringbone reconstruction on Au(111) provides additional nucleation sites for nucleation and growth of the $[BMP]^+[TFSI]^-$ 2D crystalline phase, in addition to the steps.

Molecular resolution STM images recorded on one domain of the well-ordered 2D crystalline phase on Au(111) are shown in Figure 2b. Analogously to Ag(111), these images reveal dots and longish protrusions (marked by symbols). Again, the dots are aligned in two directions (depicted by dashed lines) along the lattice vectors of the unit cell. Similarly to the findings for Ag(111), the ratio between round and longish protrusions is 1:2. Thus, identical to Ag(111), one dot and two longish features are proposed to represent an anion-cation pair (dots: alkyl chains of the cation pointing upward from the surface; longish features: two CF_3 groups per anion). However, different from Ag(111), every third row along the $\vec{A}$ lattice direction shows dimers (two dots next to each other), which are slightly rotated against this direction, rather than single dots. This leads to a twofold higher density of dots than in the lines on Ag(111) or in the other two parallel lines on Au(111). In the other two of these lines, the arrangement of the dots and their density closely resembled that on Ag(111). Between these latter lines there are pairs of longish protrusions, which are aligned in the same direction and with the same distance as the dots. The longish features have the same direction on both sides of the dimer rows, while between the other two lines featuring single dots they are rotated by ~ 120°. In the monolayer coverage regime, the adlayer unit cell has a size of $|\vec{A}| = 3.8 \pm 0.2$ nm and $|\vec{B}| = 2.9 \pm 0.2$ nm, with an angle of $78 \pm 5°$ between the adlayer lattice

vectors, which approximately corresponds to a commensurate $\begin{bmatrix} 13 & 0 \\ 8 & 11 \end{bmatrix}$ unit cell. In the (sub-)monolayer regime the unit cell is larger, with $|\vec{A}| = 4.2 \pm 0.2$ nm and $|\vec{B}| = 3.4 \pm 0.2$ nm, with an angle of 68 ± 5° between the adlayer lattice vectors, which approximately corresponds to a $\begin{bmatrix} 15 & 0 \\ 11 & 13 \end{bmatrix}$ unit cell, indicating that at (sub-)monolayer coverage the phase is slightly expanded (cf. ref.[21,22]). In total, the unit cell contains 8 dots and 16 longish protrusions (8 anion-cation pairs). For more details see our previous publications.[21,22]

3. $[BMP]^+[TFSI]^-$ | HOPG

Next we discuss the structure formation behavior of an adsorbed $[BMP]^+[TFSI]^-$ (sub-)monolayer on HOPG at ~ 100 K. The large-scale STM micrograph in (Figure 1c) reveals an anisotropic long-range ordered 2D crystalline phase, which looks different than those on Ag(111) and Au(111). The structure is characterized by parallel rows of IL adsorbates (the direction of the rows is marked by a yellow arrow). In addition, the 2D crystalline phase exhibits missing rows (decreased apparent heights) with varying distances, which is most likely related to translational domain boundaries between two independently growing islands / domains, indicating that these islands cannot rearrange when they approach each other. Besides the well-ordered 2D crystalline phase, we also observed areas close to the missing rows, which exhibit a more pronounced disorder, pointing to weaker affective interactions between neighboring rows than on Ag(111) or Au(111). Furthermore, even when using mild tunneling conditions (~ 10 pA, U ~ -1V), the 2D crystalline phase usually disappeared after one or a few scans in this area (the STM tip displaces the molecules), which points to a rather weak corrugation in the adsorbate-substrate interactions.[26]

Even though the 2D crystalline phases on Ag(111) and Au(111) are different in their arrangement, they show the same molecular features (dots and longish protrusions). On

HOPG at 100 K, in contrast, the 2D crystalline phase appears very different (Figure 2c). In this case the structure consists of parallel molecular rows, exhibiting slightly different apparent heights, which could be related to different adsorption sites with respect to the underlying HOPG atomic lattice. As depicted in Figure 2c, the average inter–row distance d_{inter} is 1.55 nm and the rows consist of elliptical features, which are oriented perpendicular to the rows, with an average intra–row distance d_{intra} of 0.80 nm. The experimental STM images point to a commensurate, rectangular $\begin{bmatrix} 6 & 0 \\ 2 & 4 \end{bmatrix}$ unit cell with the dimensions 8.58 Å × 14.86 Å, with the lattice vectors pointing along the zig-zag[74] direction and along the armchair[74] direction (depicted by a yellow dashed line), respectively.

The elliptical features are assigned to the cations, which are lying flat on the HOPG surface. The rows are aligned along the armchair axis of the surface, the elliptic features in the rows are oriented along the direction of the zig-zag axis. The anions are not visible in the STM images, which we attribute to their low density of states close to the Fermi level (see section 5). This will be discussed more together with the corresponding DFT-D calculations, which will be shown and described in Figure 3 (see section III.A.5). For more details we refer to ref.[26]

4. $[BMP]^+[TFSI]^-$ | Cu(111) and TiO_2(110)

In contrast to the well-ordered 2D molecular assemblies observed on Ag(111), Au(111) and HOPG, no long-range ordered 2D arrangements were observed on the more reactive Cu(111) and rutile TiO_2(110) surfaces after similar deposition procedures. The STM image of a $[BMP]^+[TFSI]^-$ (sub-)monolayer on Cu(111) (Figure 1d), was recorded after vapor deposition on the sample held at ~ 200 K (STM imaging at ~ 100 K). An adsorption temperature significantly below r.t. was chosen in order to avoid IL decomposition (to be discussed in section C). Under these conditions, the IL adsorbates are agglomerated into islands with

relaxed dendritic shapes, which are homogeneously distributed over the terrace. The different arrangement of the adsorbed ILs on Cu(111) as compared to Ag(111) and Au(111) most likely results from a different balance between stronger adsorbate-substrate interactions and adsorbate-adsorbate interactions. This could lead to a different intramolecular conformation of the adsorbed IL anion-cation pairs. The absence of an ordered structure is, however, related to kinetic effects caused by more pronounced surface diffusion barriers, which hinder the IL adsorbates to reach a well-ordered, stable configuration at the present, lower adsorption temperature. Lower adsorption temperatures are required due to the increasing tendency for IL decomposition on this more reactive surface at higher temperatures. This is elucidated in more detail in ref.[24]. Molecular resolution STM images of an adsorbed $[BMP]^+[TFSI]^-$ monolayer on Cu(111) at 100 K (Figure 3a) show that the islands consist of features with different forms (roundish and elliptical protrusion). These structures, can, however, not be assigned to specific molecular features at present.

Inspection of a $[BMP]^+[TFSI]^-$ covered rutile TiO_2(110) surface (Figure 1e) mainly revealed that the appearance of the surface changed. STM images of the (1 × 1) structure of the pristine surface are dominated by one-dimensional lines along the [001] direction, which are made-up by Ti^{4+}-ions appearing with an increased apparent height, while bridged oxygen atoms show up as indentation, due to electronic effects.[28,75] The large-scale STM image of the IL covered TiO_2(110) surface in Figure 1e does not show the characteristic rows of the TiO_2(110) surface. Apparently, the STM corrugation is damped by the IL adlayer. Only in the small-scale STM images of an adsorbed IL adlayer on TiO_2(110) (Figure 3b) we could resolve protrusions which are aligned along the [001] direction of the substrate, with the difference between the lines of ~ 0.61 nm being close to that observed for the TiO_2(110) surface (~ 0.63 nm[75]). Along the rows the distance between the protrusions is around 0.61 ± 0.07 nm, which is significantly larger than the distance between maxima in the pristine

TiO_2(110) surface (~ 0.3 nm). The diameter and density of the features in Figure, 4b are 0.56 ± 0.06 nm (full width at half maximum) and 2.6 ± 0.4 nm^{-2}, respectively. Obviously, these features are aligned along the atomic rows in [001] direction, but because of their larger distance along this direction they cannot reflect the TiO_2(110) lattice. Instead, they must be due to the adlayer. On the other hand, due to their small size and mean distance, we can exclude that one protrusion represents a complete ion pair, considering that the cation related dots on Ag(111) are approximately 1.15 nm apart. Therefore, a molecular level assignment of the adlayer structure resolved in the STM image in Figure 3b cannot be given at present (see also ref.[28]) Thus, different from $[BMP]^+[TFSI]^-$ (sub-)monolayers adsorbed on the Ag(111), Au(111) and HOPG surfaces in Figure 2, adsorbed anions and cations could not be identified on the Cu(111) and TiO_2(110) surfaces. The XPS measurements, however, (see Figure 6 and 7) reveal intact adsorbed anion-cation pairs (see below) at least in the low temperature regime.

5. DFT-D calulations of $[BMP]^+[TFSI]^-$|Ag(111) and HOPG

DFT-D3 calculations of a single, quasi-isolated $[BMP]^+[TFSI]^-$ ion pair in a (5×5) overlayer structure on Ag(111) (lattice vector of the surface unit cell of the adlayer: 14.73 Å) or in a (6x6) overlayer structure on graphite(0001) (lattice vector of surface unit cell of overlayer structure: 14.83 Å) show that they form stable adsorption structures, in which $[BMP]^+$ and $[TFSI]^-$ adsorb side by side (Figure 4c and f). In both cases $[TFSI]^-$ adopts a cis-configuration with respect to the S-N-S plane. Its oxygen atoms point towards the surface and the trifluoromethyl ($-CF_3$) groups are pointing upwards from the surface. The S-N-S plane is nearly parallel to the surface at a vertical distance of 3.3 Å or 3.8 Å above the uppermost layer of Ag or C atoms, respectively. As far as $[BMP]^+$ is concerned, the pyrrolidinium ring adopts an envelope conformation, i.e., the four C atoms of the ring are coplanar and the ring N atom points out of the plane. The plane of the C ring atoms adsorbs roughly parallel to the surface at a vertical distance of 3.7 Å or 3.5 Å above the uppermost layer of Ag or C atoms,

respectively. The butyl group can be in an axial position with respect to the pyrrolidinium ring and is thus oriented normal to the surface, or it can be in an equatorial position with respect to the pyrolidinium ring. In the latter case it is oriented parallel to the surface. On both substrates the equatorial position of the butyl group leads to a more stable adsorption structure (ΔE_{ad} = -0.3 eV on Ag(111), ΔE_{ad} = -0.15 eV on graphite(0001)) due to stronger van der Waals interactions with the substrate (see Table 1). In fact, dispersion interactions are dominant for the adsorption of the ionic liquid pair on Ag(111) and graphite(0001), and pure RPBE energies suggest even no stable adsorption for $[BMP]^+[TFSI]^-$ in these adsorption structures.

In total, the adsorption of an isolated $[BMP]^+[TFSI]^-$ ion pair on Ag(111) is about 0.46 eV (for the butyl group in the equatorial position) or 0.31 eV (for the butyl group in the axial position) stronger than on graphite due to the larger polarizability and thus a larger van der Waals coefficient of Ag compared to C. Although the equatorial position of the butyl group of $[BMP]^+$ is more favorable for the adsorption of the quasi-isolated ion pair, there is considerable experimental evidence that in the adlayer structures the butyl group occupies the axial position of $[BMP]^+[TFSI]^-$ on Ag(111). It has been observed experimentally that the appearance and size of the unit cells in closely related IL adlayers with different alkyl groups of varying lengths, i.e., octyl and ethyl groups in $[OMIM]^+[TFSI]^-$, $[EMIM]^+[TFSI]^-$,[25] are nearly identical, which points to vertically oriented alkyl chains. Indeed, the simulated STM image of the individual ion pairs in a (5×5) unit cell of $[BMP]^+[TFSI]^-$ on Ag(111), in which the axial position of the butyl group of $[BMP]^+$ is realized (see Figure 4c), shows one dot and two longish protrusions per ion pair (see Figure 4b) in a pattern that closely resembles the features observed in the experimental STM images (see Figure 4a). As illustrated by the superimposed ball-and-stick representation of the ionic liquid, the dots in the images of Ag(111) are due to the vertically oriented butyl group of $[BMP]^+$, whilst the two longish protrusions can be related to the two $-CF_3$ groups of $[TFSI]^-$. Although we did not calculate

the structure formation of $[BMP]^+[TFSI]^-$ in the saturated adlayer on Ag(111) observed in adsorption experiments, it seems that the calculations of individual $[BMP]^+[TFSI]^-$ ion pairs in a (5×5) unit cell on Ag(111) can be used to explain the main features of the experimental STM images.[20.]In contrast to the adsorption on Ag(111), there is no evidence that the alkyl chain of $[BMP]^+$ adopts a vertical orientation if the ionic liquid is adsorbed on HOPG.

For HOPG, we also calculated the adsorption structure in a saturated adlayer, using the unit cell that has been derived from experimental STM images. In these calculations we assumed that the butyl group of $[BMP]^+$ is arranged in the equatorial position. Calculations of this adsorption structure reveal that $[BMP]^+$ and $[TFSI]^-$ are alternately aligned in a row (see Figure 4f). Furthermore, there is a slight preference for row structures in which the horizontally oriented alkyl chain of $[BMP]^+$ cations is oriented along the zig-zag axes of graphite. In the adsorption structure the distance of the N atom of the adsorbed $[TFSI]^-$ from the surface is about 5.6 Å. This distance is significantly longer than in the quasi-isolated adsorbed ion pair on graphite(0001) (3.9 Å). The STM image simulated for this adsorption structure (Figure 4e) agrees well with the experimental ones in Figure 4d. According to the superimposed ball-and-stick representation of the IL, the longish features in the images of HOPG result from the horizontally oriented butyl group of adsorbed $[BMP]^+$, whilst the adsorbed $[TFSI]^-$ ion is nearly not visible due to the low density of states close to the Fermi level.[26].

The adsorption energy for the saturated adlayer structure is about E_{ad} = -1.49 eV with respect to an isolated ion pair, where about half of it is due to interactions between $[BMP]^+[TFSI]^-$ and graphite, which are dominated by dispersion interactions, and the other half is due to interactions between neighbored ion pairs (40% dispersion, 60% electrostatic interactions). For the latter, interactions between ion pairs within the rows are dominant, while the interactions between adjacent rows are rather small (5 meV).

Interestingly, as deduced from the experiment (explained above), $[BMP]^+[TFSI]^-$ adsorbs in a dense layer with a vertically oriented butyl group on Ag(111), while a row like structure with horizontally oriented butyl groups of $[BMP]^+[TFSI]^-$ has been found on graphite(0001). The reason for that has not been totally clarified yet. Image potential effects in the interaction with charged species should be larger for the Ag(111) metal surface than for the semimetal graphite, which makes the adsorption of a dense layer of anions and cations more favorable in the former case.

Evidence for subtle electronic differences can already be seen in slight differences in the geometries of the quasi-isolated adsorbed ion pairs on Ag and graphite: on graphite the $[TFSI]^-$ conformation has almost the same dihedral angles as the meta-stable cis-conformation of the gas phase structure (Figure 4f). In contrast, on Ag(111), $[TFSI]^-$ adsorbs about 0.5 Å closer to the surface and the dihedral angles are distorted in a way that all four oxygen atoms of the SO_2-groups point towards Ag atoms (Figure 3c).

Table 1. Total adsorption energies (RPBE-D3), adsorption energies according to pure RPBE (RPBE) and adsorption energies due to dispersion forces (D3) of quasi-isolated $[BMP]^+[TFSI]^-$ on Ag(111) and graphite(0001), with the butyl group of $[BMP]^+$ occupying either the axial (first row) or the equatorial (second row) position. All energies are given in eV and calculated compared to ion pairs in vacuum.

	Ag(111)			**graphite(0001)**		
	RPBE-D3	RPBE	D3	RPBE-D3	RPBE	D3
axial	-1.25	+0.53	-1.78	-0.94	0.26	-1.20
equatorial	-1.55	+0.70	-2.25	-1.09	0.54	-1.63

5. Comparative discussion of the structure formation of $[BMP]^+[TFSI]^-$ (sub-) monolayers

First of all the data presented above clearly indicate that reversible adsorption and desorption of intact ion pairs is only possible on the noble metal surfaces Ag(111) and Au(111), and on HOPG, whereas on Cu(111) and TiO_2(110) the adsorbed ion pairs tend to decompose at elevated temperatures. These decomposition processes will be explored and discussed in more detail in section B.

Focusing on the structure formation of the intact adsorbed ion pairs, the large-scale STM images in Figure 1 reveal rather different tendencies for structure formation on the different surfaces. On Ag(111), weakly attractive adsorbate – adsorbate interactions and a low barrier for surface diffusion result in a long-range ordered 2D crystalline structure at ~ 100 K, which tends to cover large areas of the silver terraces in a single domain. On the Au(111) surface, the 2D crystalline phase is not only limited by steps, but also by the bending points of the herringbone surface reconstruction. Furthermore, we also observed coexisting islands of the 2D crystalline phase at submonolayer coverage, which did not exist on Ag(111). Adsorbate-adsorbate interactions lead to the formation of a 2D crystalline phase on HOPG as well, which, however, appears rather different than on Ag(111) and Au(111). On the more reactive Cu(111) surface, IL adsorbates were found to agglomerate into islands with relaxed dendritic shapes, with no long-range order. Finally, also on rutile TiO_2(110) we did neither observed an ordered adlayer structure nor could we identify anions and cations in the adlayer could not be given.

In the molecular-resolution STM images, we unambiguously identified IL anion-cation pairs for adsorbed $[BMP]^+[TFSI]^-$ (sub-)monolayers on Ag(111), Au(111) and HOPG at 100 K. Even though the 2D arrangements of the molecular features appear differently on Ag(111) and Au(111), the high-resolution images resolve similar molecular scale features on

both surfaces, consisting of dots and longish protrusions. These are assigned to the alkyl chains of the $[BMP]^+$ cations (dots), pointing away from the surface, and to the CF_3 groups of the $[TFSI]^-$ anions (longish protrusions), respectively, which also point upward. The STM images on HOPG, in contrast, reveal only longish features, which are aligned in molecular rows and which are assigned to the $[BMP]^+$ cations, which are lying flat on the surface.

The DFT-D calculations revealed that the IL-substrate interaction of quasi-isolated adsorbed $[BMP]^+[TFSI]^-$ on Ag and graphite are dominated by van-der-Waals interactions. In the actual adlayer structure on HOPG half of the total adsorption energy is due to IL-substrate interactions. The other half of the total adsorption energy is due to adsorbate – adsorbate interactions between the IL pairs that are almost equally composed of dispersion (40%) and electrostatic (60%) interactions. As far as the adsorption structure is concerned, on HOPG the adsorbed $[TFSI]^-$ anions mainly retain their optimal dihedral angles of the cis-conformation in the gas phase. On Ag(111), in contrast, the dihedral angles of adsorbed $[TFSI]^-$ are slightly distorted, i.e., the four oxygen atoms of the two $–SO_2$ groups of each anion point directly toward the Ag atoms. Thus there are subtle geometric differences between the adsorption structures on HOPG and Ag, which must be due to slight differences in the electronic properties. They might be a possible explanation for the rather different structural arrangements on the two surfaces.

B. Thermal stability and decomposition of $[BMP]^+[TFSI]^-$ (sub-)monolayers

In this second part we focus on the thermal stability of IL adlayers, which was monitored by XPS. To begin with we show representative XP spectra of an adsorbed Li-free $[BMP]^+[TFSI]^-$ multilayer on HOPG at r.t. (no decomposition) in Figure 5, which can serve as reference for the following XPS measurements. The peak positions in the XP core level spectra are listed in Table 2. To indicate the origin of the different peaks in the XP spectra, we will use abbreviations such as F_{anion}, O_{anion}, N_{anion}, N_{cation}, C_{anion}, $C_{hetero/cation}$, $C_{alkyl/cation}$ and

S_{anion}. The presence of intact adsorbed $[BMP]^+[TFSI]^-$ is indicated by the almost 1 : 1 intensity ratio of the N_{cation} and N_{anion} peaks and the 2 : 4 : 5 intensity ratio of the C_{anion} : $C_{hetero/cation}$: $C_{alkyl/}$ peaks, which is in good agreement with the stoichiometry of the IL.[20,21,23,26,28]. For $[BMP]^+[TFSI]^-$ (sub)monolayers, however, slightly different values for the BE are observed depending on the substrate. In the presence of Li ions, more pronounced BE shifts are expected (to be discussed below).

Table 2. Binding energies of different XPS peaks for an adsorbed $[BMP]^+[TFSI]^-$ multilayer on HOPG. Abbreviations as given in the right column will be used to refer to peaks in all following XP spectra.

Element/orbital	BE / eV	Chemical environment	denoted as
C 1s	286.0	(–C–C–),	$C_{alkyl/cation}$
C 1s	287.3	(–C–N–)	$C_{hetero/cation}$
N 1s	400.0	(–C–N–)	N_{cation}
C 1s	287.3	(–C–N–)	$C_{hetero/anion}$
C 1s	293.5	$C–F_3$	C_{anion}
N 1s	403.3	(–C–N–)	N_{anion}
F 1s	689.4	$C–F_3$	F_{anion}
O 1s	533.2	$–SO_2–$	O_{anion}
S $2p_{3/2}$	169.6	$–SO_2–$	S_{anion}

In the following, we discuss results of STM and XPS measurements on the thermal stability of $[BMP]^+[TFSI]^-$ adlayers. In general, slow annealing and simultaneous STM imaging revealed that the (2D) crystalline phases melt reversibly in the temperature interval between 170 and 235 K, on Ag(111)[20] and Au(111),[22] and the terraces appear more noisy at higher temperatures (see ref.[23]), which is related to mobile adsorbed species in a 2D gas / liquid phase that diffuse too fast to be visualized by STM. Going to higher temperatures, $[BMP]^+[TFSI]^-$ (sub-)monolayers desorb without decomposition from Ag(111) and Au(111) at ~ 500 K, as indicated by the remaining contamination-free (clean) surfaces in the subsequent STM images at r.t.

The XP core level spectra of adsorbed $[BMP]^+[TFSI]^-$ (sub-)monolayers on Ag(111),[20] Au(111),[21] and HOPG[26] at r.t. and on Cu(111)[23,24]and TiO_2(110)[28] at 80 K reveal anion-cation pair related peaks as illustrated in Figure 5. Upon increasing the temperature, the IL-related peaks disappear between 450 – 500 K on Ag(111), Au(111) and HOPG (desorption), while on the more reactive Cu(111) and TiO_2(110) surfaces more complex changes are observed, which will be discussed in the following sections.

1. $[BMP]^+[TFSI]^-$|Cu(111)

STM images and selected core level spectra of an adsorbed IL adlayer on Cu(111) recorded at 100 K before and after annealing to ~350 K are shown in Figure 6 (left). After annealing to ~ 350 K the STM images on Cu(111) look clearly different than on Ag(111) and Au(111) at r.t., which are characterized by mobile species in a 2D gas / liquid phase. For Cu(111) we find well-ordered 2D islands, either attached to the steps or on the terraces (Figure 6, upper image, right). In addition, the steps on Cu(111) are modified and their orientation changes by ± 120°(step faceting), as marked by dashed lines in that image.[23] The high stability of the 2D islands together with their relatively high aspect ratio point to strong, anisotropic interactions between the adspecies. The dimensions of the adlayer unit cell are $|\vec{A}| = 0.47 \pm 0.02$ nm and $|\vec{B}| = 0.52 \pm 0.02$ nm and $\alpha = 90 \pm 2°$ (marked in Figure 6, lower image, right), which results in a commensurate adlayer structure, which is in standard matrix notation described by a $\begin{bmatrix} 2 & 1 \\ 0 & 2 \end{bmatrix}$ superstructure. The dimension of the unit cell is by far too small for a $[BMP]^+[TFSI]^-$ adlayer and therefore we assume that these islands arise from decomposition products. It may be related to the pseudo-(100)-S phase, which was reported to form as metastable structure on Cu(111).[76]

Beside the structural information gained by STM, the chemical state of the surface was probed by XPS at 80 K, after deposition at 200 K and during cool-down after annealing to ~ 350 K (Figure 6, lower part). For example, before annealing (XPS spectra with turquois-shaded areas) the adsorbed $[BMP]^+[TFSI]^-$ (sub-)monolayer on Cu(111) shows F 1s and S 2p core level signals with the characteristic F_{anion} peak and the S_{anion} doublet of molecular adsorbed $[BMP]^+[TFSI]^-$. After annealing to ~ 350 K, the spectra change considerably (Figure 6, XPS spectra with yellow-shaded areas). Now, the F_{anion} peak and the S_{anion} doublet reveal significant chemical shifts to lower BEs (F 1s ~ 1eV, S 2p ~ 2eV). In addition, another S 2p doublet evolves at ~ 162 eV. Due to the large shift of the S_{anion} doublet, we assign this and the new doublet to the formation of two new adspecies. The low-BE doublet (162.5 and 161.3 eV) is assigned to adsorbed atomic sulfur (S_{ad}) or to Cu_xS,[76] which may be responsible for the square commensurate adsorbate structure resolved in the STM image in Figure 6 (upper image, right) (see also above). The second doublet at 168.0 and 166.8 eV probably stems from adsorbed SO_x.[77] Such species are expected to be mobile on the surface at r.t., forming a 2D gas / liquid phase, accordingly they do not show up as second adlayer structure in STM images, but only as noisy features on the terraces. We note that upon cooling to 100 K, we observe condensation of these species, e.g., at the perimeter of the ordered 2D islands (not shown). In total, the combination of STM and XPS measurements shown in Figure 6 demonstrates that upon annealing a $[BMP]^+[TFSI]^-$ adlayer on Cu(111) to slightly above r.t. (~ 350K), the $[TFSI]^-$ anions decompose into fragments such as Cu_xS (or S_{ad}), SO_x, and probably other fluorine- and carbon-containing species like $CF_{3,ad}$,[23] whereas the $[BMP]^+$ is expected to be more or less stable up to ~ 350 K (no significant changes in the C 1s peak around 285 eV, mainly a small increase of C_{alkyl} peak most likely due to decomposition of CF_3 species from the anion).

2. $[BMP]^+[TFSI]^-|TiO_2(110)$

In a similar way we investigated the thermal stability of $[BMP]^+[TFSI]^-$ adlayers adsorbed on $TiO_2(110)$ in annealing experiments, covering the temperature regime between r.t. and ~ 600 K. After each annealing step, the surface composition was analyzed by XPS. In Figure 7, we display selected detail spectra of different spectral regions (F 1s, S 2p, and N 1s; note: only the N 1s peak at ~ 404 eV refers to the cation) recorded after annealing a 1.5 ML $[BMP]^+[TFSI]^-$ film to the temperatures indicated in Figure 7.[28]

Starting at 300 K, all spectra show an overall loss in intensity in all peaks, which, in the beginning, is most likely due to desorption of molecules in the second layer. For temperatures exceeding ~ 400 K, decomposition of $[BMP]^+[TFSI]^-$ molecules plays an increasingly important role, which is indicated by the disappearance or shifts of peaks and the appearance of new peaks in the spectra.

In the N 1s region (middle of Figure 7), the $[BMP]^+$ related N_{cation} peak at ~ 400 eV shifts slightly, by about 0.3 eV, to lower BE before it completely disappears at 600 K. The N_{anion} peak experiences a much stronger shift to lower BE, by about ~ 2.0 eV at 500 K. This peak shift is much more pronounced than those observed in the F 1s and S 2p anion signals and consequently, we assigned the N 1s peak formed at 500 K to a decomposition product of the adsorbed $[TFSI]^-$ anion. Based on its BE of ~ 397 eV, the peak could be representative for TiN_x species; BEs of TiN_x are known to be around 397.1 to 397.4 eV.[78] Finally, we note that this peak and also the N 1s contribution related to the cation start to vanish at 300 K and have completely disappeared at 590 K (see also below).

The spectra in the F 1s and in the S 2p regime (left and right panels in Figure 7) show a very similar behavior. The F_{anion} and S_{anion} peaks strongly decrease in intensity between 410 and 500 K, and shift to lower BE (about 1 eV). Furthermore, new features appear at significantly lower binding energies. For the S 2p region, a new peak doublet (with BEs of

161.3 eV and 162.6 eV) starts to grow in at 500 K, which is (based on findings by Rodriguez et al.[79]) assigned to sulfur adsorbed in oxygen vacancies on TiO_2(110). Peaks at those BEs were also detected during the decomposition of $[BMP]^+[TFSI]^-$ on Cu(111) and assigned to S_{ad} species.[76,80] In good agreement with findings and interpretation by Hebenstreit et al.,[81,82] we assume that S_{ad} reacts with the titania surface at T > ~ 450 K by replacing bridge-bonded oxygen by sulfur species.

In the F 1s region the original F_{anion} peak shifts by 0.9 eV to lower BE between 300 and 500 K and concomitantly decreases in intensity. At 410 K a new peak appears at 684.6 eV, which grows in intensity at the expense of the F_{anion} peak. We suggest that the new species corresponds to fluorine atoms (F_{ad}) adsorbed on TiO_2(110).[28] Note that the original F 1s peak and also the respective C 1s species from the C-F bond at ~ 292 eV have completely vanished at less than 620 K. This means that part of the decomposition products of the $[TFSI]^-$ anion containing fluorine and sulfur has desorbed from the surface, whereas the remaining part has reacted with the substrate by forming either adsorbed F_{ad} or S_{ad} species or by filling oxygen vacancies on TiO_2(110). Nitrogen containing decomposition products (both from the anion as well as from the cation) seem to have completely desorbed (within the detection limit), not even TiN_x species, which may be formed during the early stage of the decomposition process, can be detected above 600 K. The $[BMP]^+$ cation seems to be more stable than the $[TFSI]^-$ anion, the reduction of the intensity of the respective C 1s (doublet at 285 eV) and the N 1s peak (403eV) is less pronounced compared to the S 2p and F 1s peaks being representative for the anion. At 500 K, where already large parts of the anions are decomposed, we still observe about 40 – 50% of the initial intensity in the XPS peaks related for the cation, although carbon-related decomposition products might also appear in these peaks. Only above 550 K the cation-related peaks decrease strongly in intensity.

Overall, the combined STM and XPS investigations of the thermal stability of $[BMP]^+[TFSI]^-$ (sub-)monolayers revealed that these IL adlayers interact weakly with inert surfaces such as the Ag(111), Au(111) and HOPG surfaces, and also desorb molecularly in the temperature range 450 – 500 K, without any measurable decomposition. On the more reactive Cu(111) and TiO_2(110) surfaces, this is different. On Cu(111), the $[TFSI]^-$ anions decompose close to r.t. (> 350 K) into fragments such as Cu_xS (or S_{ad}) and probably other species, forming (at least partly) a stable commensurate adsorbate structure, whereas the cation seems to be stable in the temperature regime, at least up to 350 K. On TiO_2(110), decomposition of adsorbed $[BMP]^+[TFSI]^-$ starts at about 400 K, displaying significant $[TFSI]^-$ decomposition into products such as TiN_x, S_{ad} and F_{ad} at ~ 500 K. Similarly to Cu(111), the $[BMP]^+$ cation is more stable than the $[TFSI]^-$ anion, the decomposition is less pronounced compared to the anion below 500 K. A strong decay of the cation related XPS signal is found only above 550 K. These finding are highly relevant for the understanding of processes at the electrode|electrolyte interface, as they show thermal decomposition already at slightly elevated temperatures for more reactive electrodes, in the absence of any potential or ion effects. Only for essentially inert surfaces such as noble metals or the base plane of HOPG adsorption is fully reversible, without measurable decomposition.

C. Surface chemistry and thermal stability of $[BMP]^+[TFSI]^-$ + Li adlayers

In this section we extend the discussion of the thermal stability of $[BMP]^+[TFSI]^-$ by including also the shuttle ion, in this case Li, as the second important part of the electrolyte. In this situation, not only the interaction with the (more or less reactive) substrate can cause reactive decomposition of the adsorbed IL, but in addition also its interaction with adsorbed Li. Considering the high reactivity of adsorbed alkali atoms, this is assumed to contribute significantly to the SEI formation in Li-ion batteries. As mentioned before, Li is deposited by evaporation as well, which is different from the situation in a battery cell. Once adsorbed on

the surface, however, it does not matter for the resulting surface chemistry whether Li arrived as cation, as it is the case in a battery cell, or as neutral atom.

1. $[BMP]^+[TFSI]^-$ + Li | HOPG

In this section we first summarize XPS results on the interaction of Li with HOPG (Figure 8), before focusing on the interaction of a monolayer of $[BMP]^+[TFSI]^-$ with Li on HOPG. Upon stepwise increasing Li vapor deposition (0.1 – 1.6 ML, for definition of a Li monolayer see experimental section) on the HOPG sample held at 80 K, the C 1s and Li 1s core level spectra reveal a gradual damping of the C 1s peak with increasing Li coverage. Simultaneously, the Li 1s spectra show the evolution of a measurable peak after the third Li dose (~ 0.5 ML) at a BE of ~ 55.4 eV and its gradual growth after each deposition step, which is attributed to increasing amounts of adsorbed Li. This data set allows also to calculate the Li deposition rate (see experimental section). We note that the C 1s substrate peak of HOPG shifts slightly in binding energy (~ 0.3 eV), which is attributed to changes in the charge transfer from Li to the uppermost graphene layers. Similar shifts have been observed for K on HOPG.[83] Virtually all deposited Li adsorbs on HOPG at 80 K. In contrast, after vapor deposition of 1 ML of Li on pristine HOPG at r.t., we only observed a featureless line (no peak) in the Li 1s range, indicating that it intercalates into the bulk of HOPG as Li^+.[27]

To generate mixed IL + Li adlayers on HOPG, Li (1.6 ML) was postdeposited on a HOPG surface covered by a preadsorbed $[BMP]^+[TFSI]^-$ (sub-)monolayer at r.t. (Figure 9). XPS spectra confirm that the Li-free adlayer (Figure 9, bottom of the panel) displays the F_{anion}, O_{anion}, N_{anion}, N_{cation} and S_{anion} peaks expected for adsorption on HOPG (see Figure 5) (note at IL (sub-)monolayer coverages the C 1s region is dominated by the HOPG substrate peak and therefore not shown). After deposition of Li (~ 1.6 ML), all adsorbate-related peaks shift to higher BEs. Furthermore, new peaks (filled yellow) emerge at the low BE side (Figure 9, top

of the panel). The new peaks are related to the decomposition of predominantly $[TFSI]^-$ anions into products such as Li_3N, LiF, Li_2S, Li_xSO_x, Li_2O, LiOH, etc..[35,36,84] Interestingly, in the presence of a preadsorbed $[BMP]^+[TFSI]^-$ (sub-)monolayer, almost all postdepostited Li remains in the surface region, as indicated by the emergence of a peak with significant intensity in the Li 1s range at ~ 56.5 eV (yellow), which is assigned to Li-containing decomposition products (metallic Li is expected at a lower BE of ~ 55.4 eV[24,27]). Its intensity is comparable with that after dosing of a similar amount of Li on HOPG at 80 K, where it was shown that no intercalation takes place.[27]. Thus, in contrast to pristine HOPG, almost all Li remains in the surface region, i.e., for present Li deposition Li intercalation is essentially inhibited by a preadsorbed $[BMP]^+[TFSI]^-$ adlayer. The energy shift of the peaks will be discussed in the following section on lithiated HOPG (section C.2.)

2. $[BMP]^+[TFSI]^-$ + Li | lithiated HOPG

Here, we focus on the adsorption of a monolayer of $[BMP]^+[TFSI]^-$ on lithiated HOPG, which was investigated by XPS and by measurements of the work function Φ using UPS (He I line) (Figure 10).

After deposition of ~ 1 ML of Li on pristine HOPG at r.t. the work function Φ is virtually identical with that of pristine HOPG (Φ = 4.8 ± 0.1 eV) (Figure 10, right panel, black solid line), further supporting that Li intercalate efficiently under these conditions. After cooling the lithiated HOPG sample (preparation by deposition of ~ 1ML of Li at r.t., see Figure 8) to 80 K, a monolayer of $[BMP]^+[TFSI]^-$ was deposited under these conditions. XPS spectra recorded subsequently are presented in Figure 10 (bottom of the left and the center panel). The N 1s spectrum looks essentially identical to that obtained for $[BMP]^+[TFSI]^-$ adsorbed on pristine HOPG (cf. Figure 9), confirming the presence of intact adsorbed anion-cation pairs. The Li 1s range displays a featureless line. The work function measurements reveal a small

increase of Φ, compared to lithiated HOPG at 80 K, reflecting a small adsorbate-induced change of the surface dipole. Afterwards, the sample was heated to r.t. and XPS and UPS spectra were acquired as a function of temperature during slow annealing. N 1s and Li 1s core level spectra (Figure 10, top of the left and center panel) as well as the work function Φ before and after heating to r.t. (Figure 10, right panel, red solid line) are given in Figure 10. Interestingly, after annealing the N 1s spectrum showed distinct modifications compared to the spectrum recorded after deposition at 80 K. Both, the N_{cation} (red) (404.3 eV) and N_{anion} (cyan) (401.1 eV) peaks shifted to higher BE by ~ +1.6 and 1.3 eV, respectively (similar shifts were also observed for all adsorbate-related XP peaks (not shown). In addition, a new peak emerged at 398.5 – 399.0 eV (yellow), which is assigned to an inorganic compound such as Li_3N, formed by the partial decomposition of the IL adlayer. Evidence for other Li-containing products, similar to those obtained after postdeposition of Li on a preadsorbed IL adlayer (cf. Figure 9), was observed in the F 1s, O 1s, C 1s and S 2p spectral ranges (shown in the Supporting Information (SI)). In addition, we found a distinct peak emerging in the Li 1s spectrum at ~ 56.5 eV, similar to the BE of the Li 1s peak observed upon Li postdeposition on a HOPG surface precovered by a $[BMP]^+[TFSI]^-$ adlayer. Simultaneously, the work function Φ showed a massive decrease by ~ –1.2 eV. Based on these findings in combination we conclude that at least a fraction of the intercalated Li^+ has deintercalated from the bulk of the lithiated HOPG and reacted with $[BMP]^+[TFSI]^-$ adsorbed on the graphite surface. The strong decrease of Φ is assigned to the accumulation of $Li^{\delta+}$ species at the surface and the corresponding changes in the surface dipole. The accumulation of $Li^{\delta+}$ species at the surface is driven by a stabilization of these species either by non-reactive, electrostatic interactions in the IL adlayer or by reactive bond formation during reactive decomposition of the IL, which results in rather stable surface species such as. Li_3N, LiF, Li_2S, Li_xSO_x, Li_2O. Accordingly, we assign the energy shift of the core level peaks related to intact adsorbed ion pairs to an

initial state effect due to the changed chemical environment of adsorbed $[BMP]^+[TFSI]^-$ by the electrostatic potential of adsorbed $Li^{\delta+}$.

Overall, the XP spectra recorded on the IL covered lithiated graphite after warm up to r.t. closely resemble those obtained after postdepositon of Li onto a preadsorbed $[BMP]^+[TFSI]^-$ (sub-monolayer) on HOPG at r.t.. Obviously, the presence of Li on the HOPG surface results in a distinct increase of the tendency for the reactive decomposition of the $[BMP]^+[TFSI]^-$ adlayer compared to pristine HOPG. Here it does not matter whether Li is deposited as neutral atom from the vacuum side or whether it reaches the surface by segregation from deeper regions in the graphite substrate.[27] In the case of deintercalation of Li^+ from the bulk of lithiated graphite, Li is stabilized at the surface due to (reactive) interaction with the adsorbed IL species, which changes the dynamic equilibrium between dissolved/intercalated Li^+ and surface Li. This interaction provides the energetic driving force for the deintercalation process.

3. $[BMP]^+[TFSI]^-$ + Li | Cu(111)

In a comparable way we investigated the interaction of a $[BMP]^+[TFSI]^-$ adlayer with Li on the more reactive Cu(111) surface. To begin with, we describe the results on the interaction of Li with the bare Cu(111) surface at r.t and at 80 K, respectively (Figure 11).

The Cu 2p and Li 1s core level spectra recorded upon stepwise vapor deposition of Li (0.3 – 2.2 ML) on Cu(111) at r.t. (for definition of a Li ML see experimental section) reveal a gradual damping of the Cu 2p doublet upon increasing the Li coverage. Simultaneously, the Li 1s spectra display the evolution of a peak at a BE of ~ 55.5 eV starting after the first Li dose (~ 0.3 ML) (red solid line) and its gradual growth with increasing deposition. This peak is attributed to increasing amounts of adsorbed Li. The data set allows for calculating the Li deposition rate (see experimental section). In contrast to HOPG, where all deposited Li

intercalates at r.t., on Cu(111) the deposited Li remains on the substrate under these conditions. After vapor deposition of very small amounts of Li (~ 0.1 ML, below the detection limit of XPS) on Cu(111) at 80 K, the STM image (~ 100 K) show roundish protrusions, which are dispersed over the surface and which are attributed either to individual $Li^{\delta+}$ adatoms or small clusters (for more details we refer to ref.[24]). We note that a small amount of features with a decreased apparent height (indentations) are also visible, which are related to adsorbed oxygen species that are typically present on bare Cu(111) surfaces.[24,29]

Next we explored the interaction between adsorbed $[BMP]^+[TFSI]^-$ and Li. To avoid effects due to purely thermal decomposition of the $[BMP]^+[TFSI]^-$ adlayer, we deposited a $[BMP]^+[TFSI]^-$ submonolayer (~ 0.6 ML) on Cu(111) at 200 K (see section A), STM imaging at ~ 100 K, followed by postdeposition of ~ 0.2 ML of Li at the same temperature. The STM images recorded on the resulting surface (Figure 12) display marked differences compared to the Li-free $[BMP]^+[TFSI]^-$ adlayer on Cu(111), which was shown in Figures 1d and 4a. After Li postdeposition we see elongated, worm-like structures with a lower apparent height of their inner part (note that the tunneling conditions are similar to those in Figures 1d and 4a). The perimeters of these structures are decorated by dot shaped protrusions. High resolution images resolve also molecular features in the inner part of the islands (see zoom images in Figure 12 with enhanced contrast); however, they cannot be assigned to certain molecular species. These structures and the apparent depression must result from the changed nature of the adspecies upon interaction with Li, since such structures were never observed in the absence of Li on the surface. We assume that during postdeposition of Li the adsorbing Li atoms either impinge on an IL island and react instantaneously, or they diffuse as adsorbed Li on the Cu(111) surface until they reach an IL islands, where they preferentially react at the island perimeter. In this picture the dots at the island perimeters are assigned to stable Li-containing adspecies.

Analogously, we probed the chemical state of the IL adlayer (~ 0.6 ML) after postdeposition of a higher amount of Li (~ 0.7 ML of Li) on Cu(111) at 80 K (Figure 12, lower panels) by XPS. F 1s and S 2p spectra recorded before Li deposition at 80 K reveal intact adsorbed ion pairs. After postdeposition of Li (Figure 11, marked by an blue arrow), the F_{anion} peak shifted by more than 1 eV to higher BEs and a new peak formed at the low BE side (686.7 eV). In agreement with previous reports[24] we assign this to LiF. The S 2p spectrum recorded before Li deposition (lower part of the panel) shows the characteristic S_{anion} doublet at 168.9 and 170.3 eV. After postdeposition of Li, the S_{anion} peak shifts slightly to higher BE, similarly as the F_{anion} peak, and a new doublet emerges at 162.0 and 163.4 eV, respectively. This new signal we attribute either to adsorbed sulfur or, more likely, to Li_2S. Thus, postdeposition of Li to a $[BMP]^+[TFSI]^-$ monolayer on Cu(111) at 80 K leads to a reactive decomposition of the $[TFSI]^-$ anions into Li-containing decomposition products such as LiF and Li_2S, etc.. Subsequent heating to > 400 K (Figure 11, marked by a red arrow), reveals that mainly the new species such as LiF and Li_2S (yellow) persist at the surface (note: carbon species related C-F bond are no longer observed), while the peaks related to adsorbed $[BMP]^+[TFSI]^-$ vanished to a large extent. The strong decrease in all carbon-related peaks indicates that also the cation largely desorbs, either intact or in fragments from the surface.[24]

4. $[BMP]^+[TFSI]^-$ + Li | TiO_2(110)

In this last section on Li induced reactive modifications of a $[BMP]^+[TFSI]^-$ adlayer, we now focus on the interaction of a $[BMP]^+[TFSI]^-$ adlayer covered TiO_2(110) surface with Li. This differs from the previous substrates in so far as one might expect reaction of Li not only with the adlayer but also with the TiO_2 substrate. This will be investigated first, by depositing Li from the gas phase on a clean TiO_2(110) surface (Figure 13). XPS spectra recorded before and after Li deposition at 80 K show that before Li deposition the Ti 2p signal is dominated by Ti^{4+} species, as would be expected. Interestingly, a small fraction of Ti^{3+} species could be

detected in XPS, see the dark grey area in the lower spectrum of the middle panel of Figure 13. The Ti^{3+} species originates from an initial partial reduction step by thermal annealing in UHV, which was necessary in order to prepare a titania substrate with a sufficient conductance for STM measurements. After depositing about 1.5 ML Li at r.t. , the electronic structure of the TiO_2(110) surface is significantly modified, it now shows a much higher amount of Ti^{3+} species (see the Ti 2p spectrum in the upper part of the middle panel in Figure 13). Obviously, upon reaction of Li with TiO_2 one electron from the Li is transferred to the Ti^{4+} cation forming Ti^{3+}.[28] The O 1s region also displays distinct changes; after Li deposition, a new peak assigned to Li_xO appears at the left part (~532.5 eV) of the main oxygen peak. The binding energy of the Li 1s signal of 56.4 eV (top part of Figure 12), which is higher than that of metallic Li (55.1 eV), also points to a cationic / positively charged Li species.

In the following, we discuss the interaction of a submonolayer (0.7 ML) of $[BMP]^+[TFSI]^-$ on TiO_2(110) with Li (~ 1.5 ML) postdeposited at low temperature (80 K) and the thermal stability of a surface layer deposited at r.t. upon annealing to temperatures of about 470 K based on XPS measurements; the respective XPS data are displayed in the upper panels and in the lower panels of Figure 14, respectively.

When depositing Li (2 ML) at 80 K on a TiO_2(110) sample largely covered by an adsorbed $[BMP]^+[TFSI]^-$ (sub-)monolayer, the shape of the Ti 2p related peaks changes considerably, along the lines discussed above. The intensity of Ti^{3+} species increase considerably, similar as for Li deposition on pure TiO_2(110) without $[BMP]^+[TFSI]^-$ (cf. Figure 13). Obviously, even in the presence of the $[BMP]^+[TFSI]^-$ adlayer and at 80 K, Li reacts at least partly with the titania substrate. This is confirmed by the appearance of an additional peak (Li_xO) in the O1s spectral range at 532.3 eV, at exactly the same BE as the peak obtained after vapor deposition of Li on TiO_2(110) in the absence of a $[BMP]^+[TFSI]^-$ adlayer.

In addition to the reaction of Li with the titania support, it also interacts with the $[BMP]^+[TFSI]^-$ (sub-)monolayer. This can be concluded from changes in the F 1s, N 1s and S 2p regions, which reflect chemical modifications in the cation (only the N_{cation} peak in the N 1s region) and in the anion (F_{anion}, N_{anion}, S_{anion}). The general decay in intensity of the IL-related peaks implies that deposited Li reacts also with the adsorbed $[BMP]^+[TFSI]^-$ species, even at 80 K. The spectra recorded after Li deposition point to the formation of decomposition products such as Li_3N and SO_x containing species (cf. refs.[84,85]), which are mainly created by decomposition of the $[TFSI]^-$ anions. In the N 1s region, a new peak appears at ~ 398 eV and in the S 2p region, a shoulder at the low BE side of the S 2p peak is formed at ~ 168 eV. In the F 1s region, a weak feature (possibly LiF) appears at lower BE (~ 685 eV). The new N 1s peak (after Li deposition) at 398.7 eV is mainly attributed to Li_3N decomposition products, which may result from the $[TFSI]^-$ anions as well as from the $[BMP]^+$ cations. Additional small contributions of nitrogen interacting with the support (formation of TiN_x species) cannot be ruled out.

Next we explored the thermal stability of mixed $[BMP]^+[TFSI]^-$ + Li adlayers on TiO_2(110) at 300 K and 470 K after deposition of a 0.7 ML $[BMP]^+[TFSI]^-$ film on the titania substrate at r.t. followed by postdeposition of Li (~ 2 ML) at the same temperature, and subsequent annealing to 470 K. The respective spectra are shown in the upper panels of Figure 14. As expected from the results at 80 K, Li reacts partly with the TiO_2(110) substrate also upon deposition at 300 K. As also expected, it also reacts with the $[BMP]^+[TFSI]^-$ adlayer. The decomposition products of the $[BMP]^+[TFSI]^-$ (sub-monolayer) seem to be similar to those formed upon interaction at 80 K, but are much higher in intensity (the intensity does not scale linearly with the amount of postdeposited Li, which was slightly lower at 80 K). In the F 1s region, the original F_{anion} peak at 689.5 eV strongly decreases in intensity and shifts by ~ 1 eV to higher BE (300 K), similar to the behavior of other peaks related to intact adsorbed ion

pairs, while at the same time a new peak grows in at ~ 685 eV. The latter is attributed to the formation of LiF. Note that from the Li 1s peak we cannot conclude on the nature of the resulting Li compound. With increasing temperature this peak increases in intensity at the cost of the F_{anion} peak (689.5 eV) and also shifts to lower BE. Similar effects (i.e., the formation of a new peak at lower BE at the cost of the anion-derived S 2p signal, and a shift of the latter one to lower BE at 470 K) are also observed in the S 2p region where the shape of the main peak (S $2p_{3/2}$ ~ 170 eV) changes dramatically. In the presence of 2 ML Li postdeposited at r.t., the main sulfur peak consists of two doublets, one related to the intact adsorbed $[TFSI]^-$ anion (+ 170 eV) and a second feature, a decomposition product, at about 168 eV. This latter one is assigned to Li_xSO_y species, which has already been observed when annealing $[BMP]^+[TFSI]^-$ on bare TiO_2(110) (see right part of Figure 7). Furthermore, an additional, but smaller feature arising at much lower BE (161.4 eV) is attributed to the formation of Li_2S and/or S_{ad} on TiO_2. After annealing to 470 K the initial S_{anion} peak (~ 170 eV) has completely vanished and only the decomposition products at ~ 168 eV and 161.5 eV are visible with roughly equal intensity.

In the N 1s region, the changes in the N_{cation} and N_{anion} peaks reflect the behavior of both ion species (cf. Figure 5). At 300 K, after addition of 2 ML of Li, both peaks shift to higher BE, but the $[BMP]^+[TFSI]^-$ related N 1s peak (the turquois peak at ~ 401 eV) in addition splits into two peaks. The new peak at lower BE (yellow, at ~ 398 eV) mainly reflects Li_xN decomposition products (it scales with the amount of deposited Li, see ref[28]), although a contribution related to TiN_x species cannot be excluded. After annealing to 470 K, the cationic N 1s signal has completely disappeared, but a small part seems to now contribute to the (slightly) increased intensity of the Li_xN peak. As discussed for Li deposition on predeposited $[BMP]^+[TFSI]^-$ (sub-)monolayers at 80 K, the latter peaks contain contributions also from a $[TFSI]^-$ decomposition product.

Interestingly, in the Ti 2p region, annealing to 470 K leads to a decrease of the Ti^{3+} signal reaching its minimum intensity at ~ 420 K.[28] It seems that the decomposition reaction of the IL adlayer reduces the concentration of Ti^{3+} species that were intercalated in the near surface region (top few nm) of the TiO_2(110) substrate, essentially by withdrawing an electron from the Ti^{3+} species and reoxidizing them to Ti^{4+}. Therefore, at this temperature the oxygen in the Li_xO species is not (co-)generated by oxygen atoms in the TiO_2(110) crystal, but solely results from the decomposition of the IL. The only other remaining species are LiF, Li_2S, Li_3N and TiN_x (= peak at 397.1 eV).

IV. Discussion

The data presented and discussed in this review lead to the following picture for the interaction of ionic liquids and specifically of the ionic liquid $[BMP]^+[TFSI]^-$, with model electrode surfaces of increasing reactivity and battery relevance, both in the absence and presence of Li.

(1) Adsorbed $[BMP]^+[TFSI]^-$ (sub-)monolayers adsorb and desorb completely, without measurable decomposition, on/from noble metal surfaces such as Ag(111) and Au(111) or on/from similarly little reactive surfaces such as HOPG, with desorption temperatures in the range between 450 – 500 K. On more reactive surfaces, reactive decomposition is activated as well at higher temperatures. On Cu(111), the $[TFSI]^-$ anions decompose close to r.t. (> 350 K) into fragments such as Cu_xS (or S_{ad}) and probably other species, forming a stable commensurate adlayer structure. On TiO_2(110), significant IL decomposition starts at 400 K, leading to $[TFSI]^-$ decomposition products such as TiN_x, S_{ad} and F_{ad}, which are clearly visible at ~ 500 K and dominate the spectra at > 550 K. The $[BMP]^+$ anion is slightly more stable compared to the $[TFSI]^-$ anion, the main decomposition process starts around 500 K. At 600 K, all peaks related to intact $[BMP]^+[TFSI]^-$ have disappeared.

(2) On the less reactive Ag(111), Au(111) and HOPG surfaces, well-ordered 2D adsorbate structures are reversibly formed in the low-temperature range (2D melting temperatures 170 – 235 K). On Ag(111) a long-range ordered 2D crystalline phase grows in very large islands / domains at 100 K, while their size is limited by antiphase boundaries on HOPG and by the herringbone surface reconstruction on Au(111), respectively. Molecular resolution STM images reveal similar molecular features for adsorbed $[BMP]^+[TFSI]^-$ on the Ag(111) and Au(111) surfaces, with anion-cation pairs appearing as a combination of one dot and two longish protrusions. On HOPG, the resulting structure looks quite different, with regularly spaced longish features arranged in parallel rows. On Ag(111) and Au(111), the above features are assigned to the alkyl chain of $[BMP]^+$ pointing upward from the surface (dot) and the two $-CF_3$ groups per of each $[TFSI]^-$ anion (longish protrusions), respectively. In contrast, on HOPG, the longish features are related to the $[BMP]^+$ cations, which are lying flat on the surface along the main crystallographic zig-zag axes of the HOPG surface, while the anions are invisible to the STM. On HOPG, $[TFSI]^-$ almost retains the optimal dihederal angles of the less stable cis-conformation in the gas phase, the IL-substrate interaction is dominated by van-der-Waals interactions (optimized by the flat lying alkyl chain of $[BMP]^+$). Interactions between IL ion pairs are about equally due to dispersion and electrostatic interactions. On Ag(111), in contrast, the dihedral angles of the $[TFSI]^-$ anions are distorted with respect to the cis-conformation in the gas phase. In this case, slight rotation around the S-N bond leads to an adsorption structure in which the SO_2 groups point exactly into the same direction and the oxygen atoms of $[TFSI]^-$ point directly toward the Ag atoms. This change in conformation may be responsible for the different adlayer structures on Ag(111) and HOPG. On the more reactive Cu(111) surface, the interplay between adsorbate-substrate and adsorbate-adsorbate interactions result in disordered IL adsorbates that are agglomerated into

islands with relaxed dendritic shapes. No long-range order was also observed on rutile TiO_2(110).

(3) For the surfaces investigated, the tendency for Li bulk dissolution / alloy formation / intercalation increases in the order Cu(111) < HOPG (activation temperature ~230 K) < TiO_2(110). In the latter case reaction with the oxide substrate to form LiO_x and Ti^{3+} species occurs already at 80 K.

(4) In all surfaces investigated (HOPG, Cu(111), TiO_2(110)), the interaction between Li and $[BMP]^+[TFSI]^-$ (sub-)monolayers leads predominantly to $[TFSI]^-$ anion decomposition, forming products such as Li_3N, LiF, Li_2S, Li_xSO_x, Li_2O, LiOH, and possibly other products. Reactive decomposition starts already at 80 K, decomposition products desorb only at > 500 K (TiO_2(110)). The relative amounts of these decomposition products, but not their nature, depend strongly on the reaction conditions, such as temperature, amount of different components (IL and Li) and the interaction of Li (e.g., intercalation, reaction) with the respective surface. Similar decomposition products have been observed by Olschewski et al. upon interaction of Li with a thick $[TFSI]^-$-based IL film on a copper foil[35] and after room temperature adsorption of different $[TFSI]^-$-based ILs on a Li-covered copper foil.[36] Obviously, this IL can react with Li also without being directly in contact with a model electrode surface. In addition, very similar products were identified in *in situ* electrochemical studies by XPS, FTIR and EDX.[56,84] The latter result also supports the relevance of our model studies of the surface chemistry at the electrode|electrolyte interface for the SEI formation in more realistic systems.

(5) In the system showing activated Li intercalation (HOPG), deintercalation of Li^+ from the bulk is possible if surface Li is stabilized by interaction with adsorbed species, which changes the equilibrium between dissolved/intercalated Li and surface Li. For lithiated HOPG, reactive interaction of surface Li with an adsorbed $[BMP]^+[TFSI]^-$ (sub-

)monolayer results in Li depletion of the bulk, the deintercalation process starts at > 230 K. Independent of the Li transport process to the $[BMP]^+[TFSI]^-$ adlayer (Li postdeposition or Li^+ diffusion from the bulk of lithiated HOPG to the surface), the resulting adlayers are composed of Li-containing $[TFSI]^-$ decomposition products and possibly adsorbed Li, which is stabilized by electrostatic interactions in the adlayer. The presence of adsorbed Li in the adlayer was identified by the Li 1s peak and by a lowering of the work function Φ and up-shifts of all IL-related core level peaks for all surfaces investigated (HOPG, Cu(111) and TiO_2), where these latter effects are more sensitive than the Li 1s spectra at low Li coverages.[24,27,28] Similar effects and decomposition products were observed also after postdeposition of Li. Obviously, it is irrelevant for the surface reaction whether Li reaches the surface from the vacuum side, by vacuum deposition, or by segregation from the bulk.

(6) While Li intercalates spontaneously upon deposition on pristine HOPG at r.t., postdeposited Li remains in the surface region if the surface is covered by a preadsorbed IL adlayer. Moreover, the decomposition products formed upon interaction of $[BMP]^+[TFSI]^-$ and Li (Li_3N, LiF, Li_2S, etc.) do not depend on the way how Li reaches the surface, either by Li postdeposition or by Li deintercalaction from the HOPG bulk. Furthermore, these species are relatively stable and are thus well able to generate a stable SEI.

Finally we would like to emphasize that the findings and insights gained in these model studies, using structurally and chemically well-defined model electrodes and studying the interaction with individual electrolyte components on an atomic/ molecular scale, are highly relevant for batteries as they reveal molecular scale details on the structure formation and the surface chemistry during the initial stage of the SEI formation, at the open circuit potential. Evidently, the purely chemical interactions present under these conditions are sufficiently

strong to induce a decomposition of the IL electrolyte, which can be considered as a first step for SEI formation.

V. CONCLUSIONS

Aiming at a detailed understanding of the fundamental processes contributing to the formation of the solid-electrolyte interphase in Li-ion batteries, we have systematically investigated the interaction of the battery relevant ionic liquid $[BMP]^+[TFSI]^-$ with different structurally and chemically well-defined model electrode surfaces under UHV conditions. In these model studies, we also examined the influence of coadsorbed Li on the IL|solid interface. Combining microscopic and spectroscopic measurements with computational studies, we could demonstrate

i) that the interaction between solid surfaces and $[BMP]^+[TFSI]^-$ often results in thermally activated decomposition of the IL, with the onset temperature depending on the respective material,

ii) that only on inert surfaces such as noble metal surfaces or HOPG the IL adsorbs and desorbs as intact ion pair, forming ordered 2D structures on these surfaces at lower temperatures, indicative of rather weak interactions between neighbored adsorbed ion pairs (adsorbate – adsorbate interactions),

iii) that for all surfaces investigated the interaction with Li results in reactive decomposition of a preadsorbed IL adlayer already at 80 K and

iv) that the resulting Li-containing decomposition products are sufficiently stable to extract intercalated Li from surfaces preloaded with Li, by modifying the reversible equilibrium between intercalated bulk Li and (stabilized) surface Li.

Overall, the present work clearly illustrates the extent of molecular scale information that can be obtained in such a model study, and their potential for an improved understanding of

the processes taking place at the interface between (model) electrodes and battery electrolytes, which is essential for the development of improved future batteries.

AUTHOR INFORMATION

Corresponding Author

*Phone: +49 (0)731/50-25451. Fax: +49 (0)731/50-25452.

Email: juergen.behm@uni–ulm.de

Notes

The authors declare no competing financial interests.

ACKNOWLEDGMENT

This work was supported by the German Federal Ministry of Education and Research in the project LiEcoSafe under contract number 03X4636C.

REFERENCES

1. T. Welton, Chem. Rev. **99,** 2071 (1999).
2. P. Wasserscheid, T. Welton, Ionic Liquids in Synthesis (Wiley-VCH, Weinheim, 2008).
3. R. D. Rogers, K. R. Seddon, Science **302**, 792 (2003).
4. M. Smiglak, J. M. Pringle, X. Lu, L. Han, S. Zhang, H. Gao, D. R. MacFarlane, R. D. Rogers, Chem.Commun **50**, 9228 (2014).
5. H.-P. Steinrück, Phys. Chem. Chem. Phys. **14, 5010** (2012).
6. H.-P. Steinrück, P. Wasserscheid, Catal. Lett. **145**, 380 (2015).
7. N. V. Plechkova, K. R. Seddon, Chem. Soc. Rev. **37**, 123 (**2008).**
8. P. Wasserscheid, W. Keim, Angew. Chem. Int. Ed. **39**, 3772 (**2000).**
9. R. Hayes, G.G. Warr, R. Atkin, Chem. Rev. **115**, 6357 (2014).
10. F. Maier, I. Niedermaier, H.-P. Steinrück, J. Chem. Phys. **146**, 170901 (2017).
11. A. Lewandowski, Journal of Power Sources **194**, 601 (2009).
12. V. Etacheri, R. Marom, R. Elazari, G. Salitra, D. Aurbach, Energy Environ. Sci. **4**, 3243 (2011).
13. M. Armand,; F. Endres, D. R. MacFarlane, H. Ohno, B. Scrosati, Nature Mater**. 8**, 621 (2009).
14. G. Girishkumar, B. McCloskey, A. C. Luntz, S. Swanson, W. Wilcke, J. Phys. Chem. Lett. **1**, 2193 (2010).

15. M. Gauthier, T.J. Carney, A.Grimaud, L. Giordano, N. Pour, H.-H. Chang,. D. P. Fenning, S. F. Lux, O. Paschos, C. Bauer, F. Maglia, S. Lupart, P. Lamp, Y. Shao-Horn, J. Phys. Chem. Lett. **6**, 4653 (2015).

16. P. Verma, P. Maire,; P. Novak, Electrochim. Acta **55**, 6332 (2010).

17. B. Scrosati, J. Garche, Journal of Power Sources **195**, 2419 (2010).

18. E. Peled, Electrochem. Soc. **126**, 2047 (1979).

19. E. Peled, D. Golodnitsky, G. Ardel, J. Electrochem. Soc. **144**, L208 (1997).

20. F. Buchner, K. Forster–Tonigold, B. Uhl, D. Alwast, N. Wagner, H. Farkhondeh, A. Groß, R. J. Behm, ACS Nano **7**, 7773 (2013).

21. B. Uhl, T. Cremer, M. Roos, F. Maier, H.-P. Steinrück, R. J. Behm, Phys. Chem. Chem. Phys. **15**, 17295 (2013).

22. B. Uhl, F. Buchner, D. Alwast, N. Wagner, R. J. Behm, Beilstein J. Nanotechnol. **4**, 903 (2013).

23. B. Uhl, F. Buchner, S. Gabler, M. Bozorgchenani, R. J. Behm, Chem. Commun. **50**, 8601 (2014).

24. F. Buchner, M. Bozorgchenani, B. Uhl, H. Farkhondeh, J. Bansmann, R. J. Behm, J. Phys. Chem. C **119**, 16649 (2015).

25. B. Uhl, H. Huang, D. Alwast, F. Buchner, R. J. Behm, Phys. Chem. Chem. Phys. **17**, 23816 (2015).

26. F. Buchner, K. Forster-Tonigold, M. Bozorgchenani, A. Gross, R. J. Behm, J. Phys. Chem. Lett. **7**, 226 (2016).

27. F. Buchner, J. Kim, C. Adler, M. Bozorgchenani, J. Bansmann, R.J. Behm, submitted (2017).

28. B. Uhl, M. Hekmatfar, F. Buchner, R. J. Behm, Phys. Chem. Chem. Phys., **18**, 6618 (2016).

29. F. Buchner, H. Farkhondeh, M. Bozorgchenani, B. Uhl, R. J. Behm, Phys. Chem. Chem. Phys. **16**, 11191 (2014).

30. M. Bozorgchenani, M. Naderian, H. Farkhondeh, J. Schnaidt, B. Uhl, J. Bansmann, A. Groß, R. J. Behm, F. Buchner, J. Phys. Chem. C **120**, 16791 (2016).

31. G. Armstrong, A. R. Armstrong, P. G. Bruce, P. Reale, B. Scrosati, Adv. Mater. **18**, 2597 (2006).

32. R. Atkin,; S. Z. El Abedin, R. Hayes, L. H. S. Gasparotto, N. Borisenko, F. Endres, J. Phys. Chem. C **113**, 13266 (2009).

33. R. Wen, B. Rahn, O. M. Magnussen, Angew. Chem. Int. Ed. **54**, 6062 (2015).

34. F. Endres, O. Höfft, N. Borisenko L. H. S. Gasparotto, A. Prowald,; R. Al Salman, T. Carstens, R. Atkin, A. Bund, S. Z. El Abedin, Phys. Chem. Chem. Phys. **12**, 1724 (2010).

35. M. Olschewski, R. Gustus, O. Höfft, A. Lahiri, F. Endres,˙ J. Phys. Chem. C **121**, 2675 (2017).

36. M. Olschewski, R. Gustus, M. Marschewski, O. Höfft, F. Endres, Phys.Chem.Chem.Phys. **16**, 25969 (2014).

37. K. R. J. Lovelock, I. J.Villar-Garcia, F. Maier, H. P. Steinrück, P. Licence, Chem. Rev. **110**, 5158 (2010).

38. T. Waldmann, H.-H. Huang, H. E. Hoster, O. Höfft, F. Endres, R. J. Behm, ChemPhysChem **12**, 2565 (**2011).**

39. R. Foulston, S. Gangopadhyay, C. Chiutu, P. Moriarty, R. G. Jones, Phys. Chem. Chem. Phys. **14**, 6054 (2012).

40. T. Cremer, M. Stark, A. Deyko, H.-P. Steinrück, F. Maier, Langmuir **27**, 3662 (2011).

41. T. Cremer, C. Kolbeck, K.R.J. Lovelock, N. Paape, R. Wölfel, P.S. Schulz, P. Wasserscheid, H. Weber, J. Thar, B. Kirchner, F. Maier, H.-P. Steinrück. Chem. Europ. J. **16**, 9018 (2010).

42. M. Sobota, Nikiforidis I., W. Hieringer, N. Paape, M. Happel, H.-P. Steinrück, A. Görling, P. Wasserscheid, M. Laurin, J. Libuda, Langmuir **26**, 7199 (2010).

43. F. Rietzler, J. Nagengast, H.-P. Steinrück, F. Maier, J. Phys. Chem. C **119**, 28068 (2015).

44. O. Höfft, S. Bahr, M. Himmerlich, S. Krischok, J.A. Schaefer, V. Kempter, Langmuir **22**, 7120 (2006).

45. A.B. Biedron, E.L. Garfunkel, E.W. Castner Jr., S. Rangan, J. Chem. Phys. **146**, 054704 (2017).

46. W. Sitaputra, D. Stacchiola, J.F. Wishart, F. Wang, J.T. Sadowski, Adv. Mat. **29**, 1606357 (2017).

47. T. Xu, T. Waehler, J. Vecchietti, A. Bonivardi, T. Bauer, J. Schwegler, P. S. Schulz, P. Wasserscheid, J. Libuda, ChemPhysChem **18**, 1 (2017).

48. T. Xu, T. Waehler, J. Vecchietti, A. Bonivardi, T. Bauer, J. Schwegler, P.S. Schulz, P. Wasserscheid, J. Libuda, Angew. Chem. Int. Ed. **56**, 9072 (2017).

49. A. Dimitrova, M. Walle, M. Himmerlich, S. Krischok, J. Mol. Liq. **226**, 78 (2017).

50. A. Lahiri, T. Carstens, R. Atkin, N. Borisenko, F. Endres, J. Phys. Chem. C **119**, 16734 (2015).

51. C. Müller, S. Vesztergom, T. Pajkossy, T. Jacob, J. Electroanal. Chem. **737**, 218 (2015).

52. T. Carstens, R. Gustus, O. Höfft, N. Borisenko, F. Endres, H. Li, R. J. Wood, A. J. Page, R. Atkin, J. Phys. Chem. C **118**, 10833 (2014).

53. A. Elbourne, S. McDonald, K. Voïchovsky, F. Endres, G. G. Warr, R. Atkin, ACS Nano **9**, 7608 (2015).

54. R. Wen, B. Rahn, O. M. Magnussen, J. Phys. Chem. C **120**, 15765 (2016).

55. Y. Fu, A.V. Rudnev, Current Opinion in Electrochemistry **1**, 59 (2017).

56. D. Aurbach, A. Zaban, Y. Ein–Eli, I. Weissman, O. Chusid, B. Markovsky, M. Levi, E. Levi, A. Schechter, E. Granot, J. Power Sources **68**, 91 (1997).

57. Y. Ando, Y. Kawamura, T. Ikeshoji, M. Otani, Chem. Phys. Lett. **612**, 240 (2014).

58. S. Kielbassa, M. Kinne, R.J. Behm, J. Phys. Chem. B **108**, 19184 (2004).

59. C. J. Powel, S., Jablonski, (National Institute of Standards and Technology, Gaithersburg, MD 2010**)**.

60. B. Hammer, L. B. Hansen, J. K. Nørskov,. Phys. Rev. B **59**, 7413 (1999).

61. S. Grimme, J. Antony, S. Ehrlich, H. J. Krieg, Chem. Phys. **132**, 154104 (2010).

62. J.D. Chai, M.HeadGordon, Phys. Chem. Chem. Phys. **10**, 6615 (2008).

63. G. Kresse, J. Furthmüller, J. Comp. Mat. Sci. **6**, 15 (1996).

64. G. Kresse, J. Furthmüller, Phys. Rev. B **54**, 11169 (1996).

65. K. Forster-Tonigold and A. Groß, J. Chem. Phys. **141**, 064501 (2014).

66. Morawietz, A. Singraber, C. Dellago, and J. Behler, Proc. Natl. Acad. Sci. **113**, 8368 (2016).

67. K. Tonigold and A. Groß, J. Comput. Chem. **33**, 695 (2012).

68. P. E. Blöchl, Phys. Rev. B **50**, 17953 (1994).

69. G. Kresse, D. Joubert, Phys. Rev. B **59**, 1758 (1999).

70. H.J. Monkhorst, J.D. Pack, Phys. Rev. B **13**, 5188 (1976).

71. E. R. McNellis, J. Meier, K. Reuter, Phys. Rev. B **80**, 205414 (2009).

72. J. Tersoff, D.R. Hamann, Phys. **31**, 805 (1985).

73. J.V. Barth, H. Brune, G. Ertl, R.J. Behm, Phys. Rev. B **42**, 9307(1990).

74. J. W. G. Wildöer, L. C. Venema, A. G. Rinzler, R. E. Smalley, C. Dekker, Nature **391**, 59 (1998).

75. U. Diebold, Surf.Sci.Rep. **48**, 53 (2003).

76. J. Jia, A. Bendounan, K. Chaouchi, V.A. Esaulov, J. Phys. Chem. C **118**, 24583 (2014).

77. R. Streber, C. Papp, M. P. A. Lorenz, A. Bayer, R. Denecke, H.-P. Steinrück, Angew. Chem. Int. Ed. **48**, 9743 (2009).

78. B. J. Burrow, A. E. Morgan and R. C. Ellwanger, J. Vac. Sci. Technol. A **4**, 2463 (1986).

79. J. A. Rodriguez, J. Hrbek, J. Dvorak, T. Jirsak, A. Maiti, Chem. Phys. Lett. **336**, 377, (2001).

80. M. Polcik, L. Wilde, J. Haase, Phys. Rev. B **53**, 13720 (1996).

81. E. L. D. Hebenstreit, W. Hebenstreit and U. Diebold, Surf. Sci. **470**, 347 (2001).

82. E. L. D. Hebenstreit, W. Hebenstreit and U. Diebold, Surf. Sci. **461**, 87 (2000).

83. P. Bennich, C. Puglia, P. A. Brühwiler, A. Nilsson, A. J. Maxwell, A. Sandell, N. Mårtensson, Phys. Rev. B **59**, 8292 (1999).

84. C. Xu, B. Sun, T. Gustafsson, K.M. Edström, D. Brandell, M. Hahlin, J. Mater. Chem. A **2**, 7256 (2014).

85. B. Lindberg, K. Hamrin, G. Johansson, U. Gelius, A. Fahlman, C. Nordling and K. Siegbahn, Phys. Scr. **1**, 286 (1970).

Figures

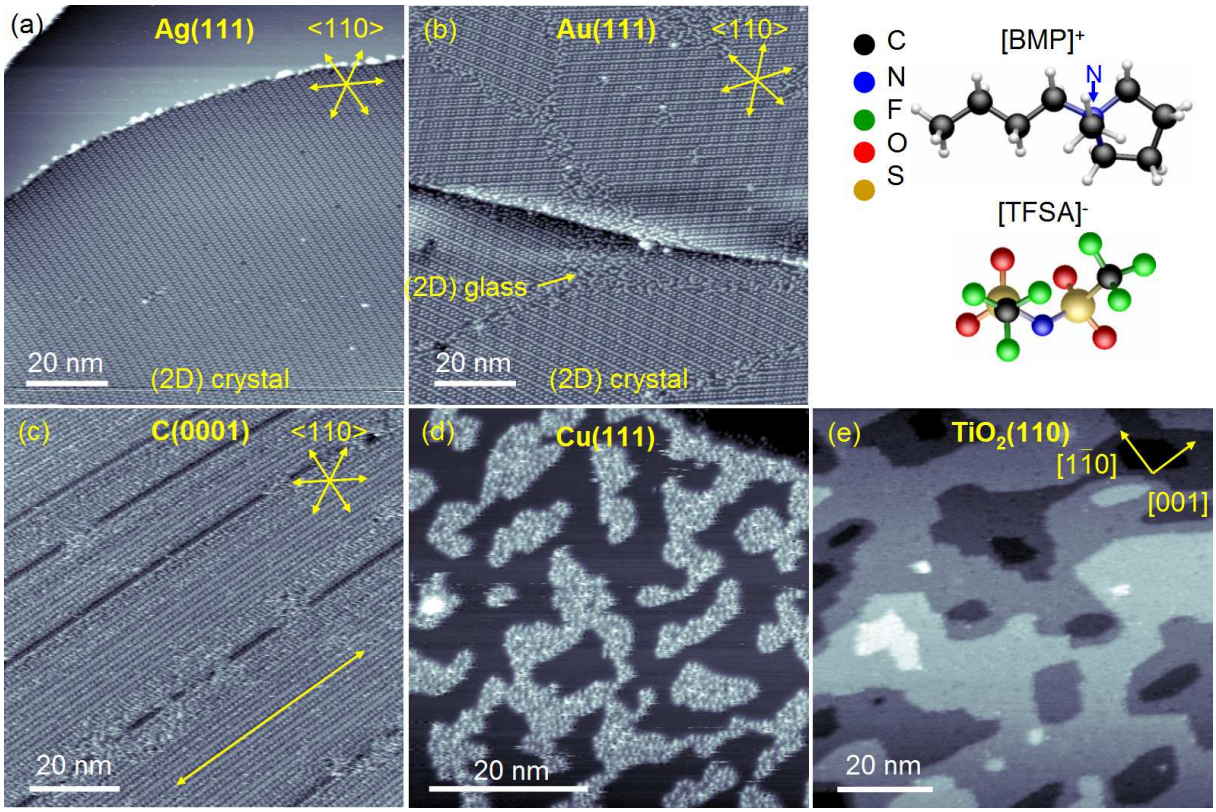

Figure 1. Large-scale STM images after vapor deposition of a $[BMP]^+[TFSI]^-$ (sub-)monolayer on Ag(111) (a), Au(111) (b), Cu(111), HOPG (d) and TiO_2(110) (e) at r.t and subsequent cooling to 100 K. On the more reactive Cu(111) surface the IL was adsorbed at 200 K to avoid decomposition. STM imaging was also conducted at 100 K. A molecular representation of $[BMP]^+[TFSI]^-$ is inserted in the Figure.

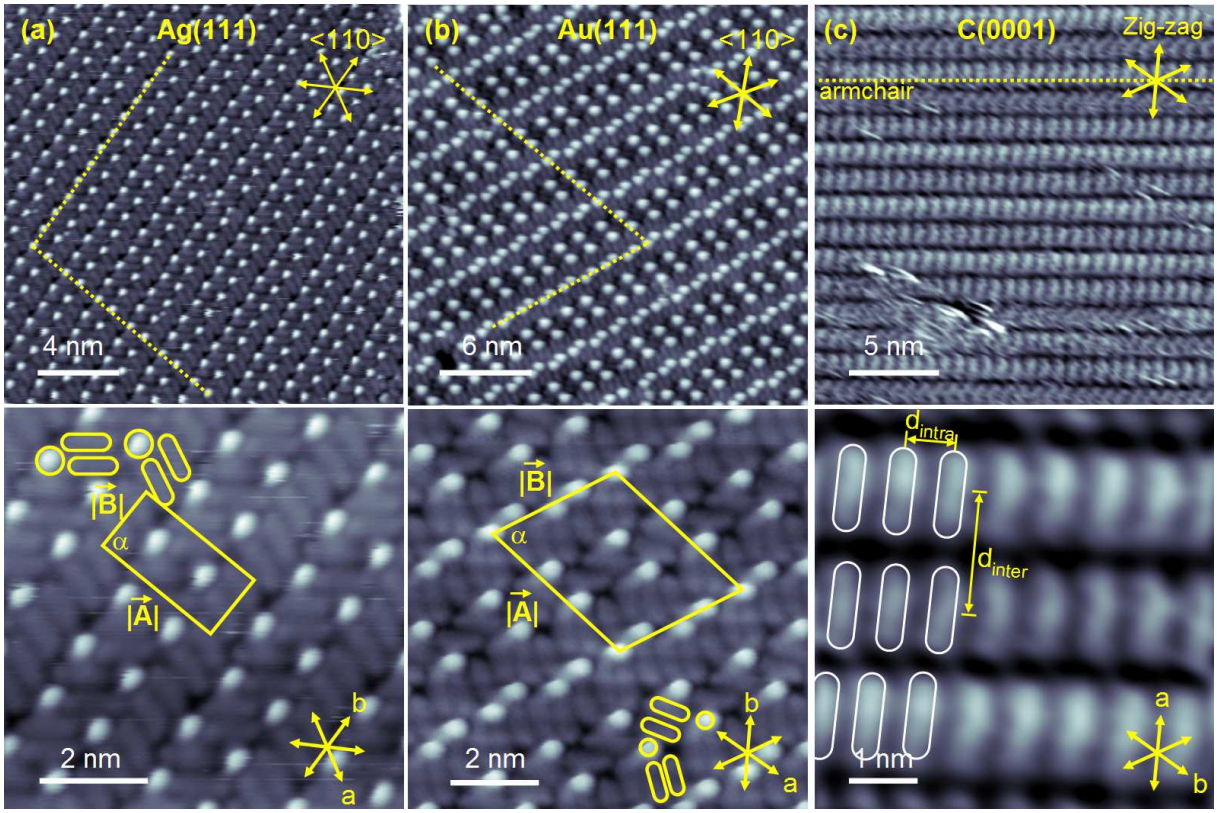

Figure 2. Molecular resolution STM images after vapor deposition of a $[BMP]^+[TFSI]^-$ (sub-) monolayer on Ag(111) (a), Au(111) (b) and HOPG (c) at r.t and subsequent cooling to 100 K.

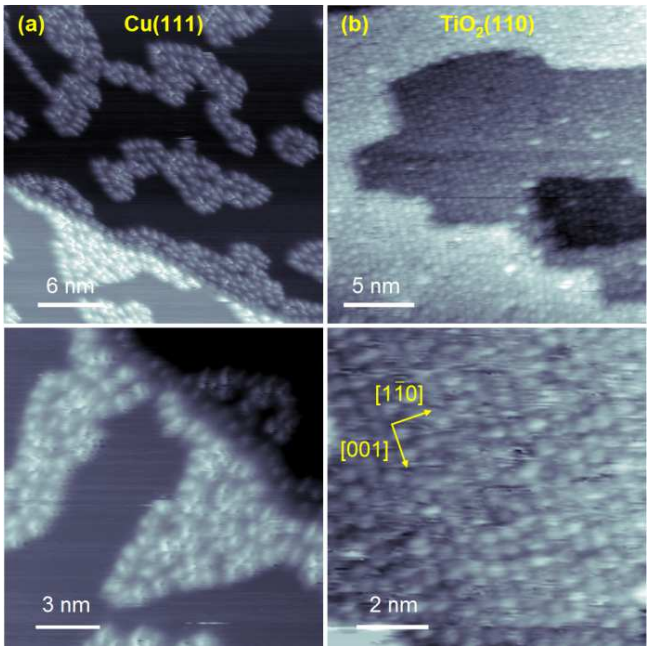

Figure 3. STM images (a) recorded at 100 K after vapor deposition of a $[BMP]^+[TFSI]^-$ (sub-)monolayer on Cu(111) at 200 K and subsequent cool-down and (b) after vapor deposition of a $[BMP]^+[TFSI]^-$ monolayer on TiO_2(110) at r.t and subsequent cool down to ~100 K.

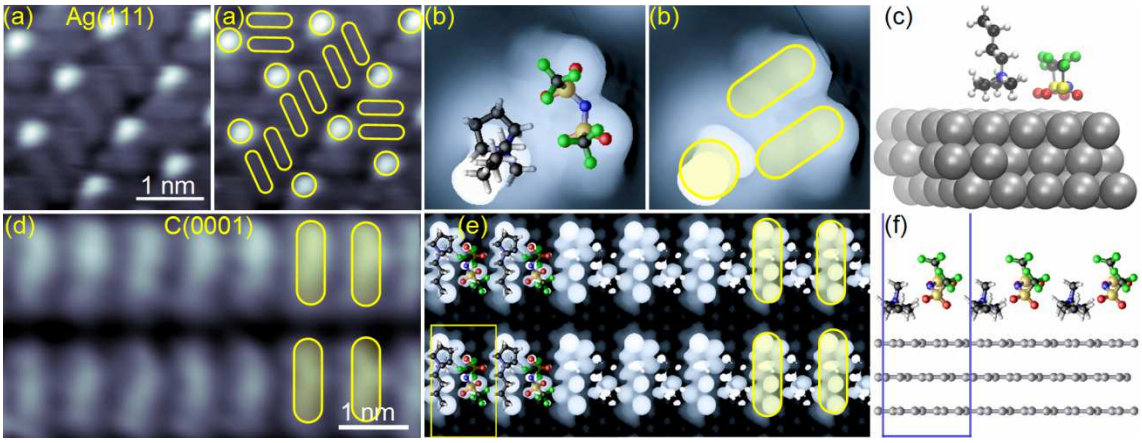

Figure 4. Experimental STM images (panel a and d) and simulated STM images derived from DFT calculations (panel b and e) of adsorbed $[BMP]^+[TFSI]^-$ on Ag(111) (upper row, panel a-c) and HOPG (lower row, panel d-f). The geometry of a quasi-isolated adsorbed $[BMP]^+[TFSI]^-$ on Ag(111) and the adsorption structure of $[BMP]^+[TFSI]^-$ on graphite(0001) in a saturated overlayer whose unit cell has been deduced from experiment are shown in panels c and f, respectively.

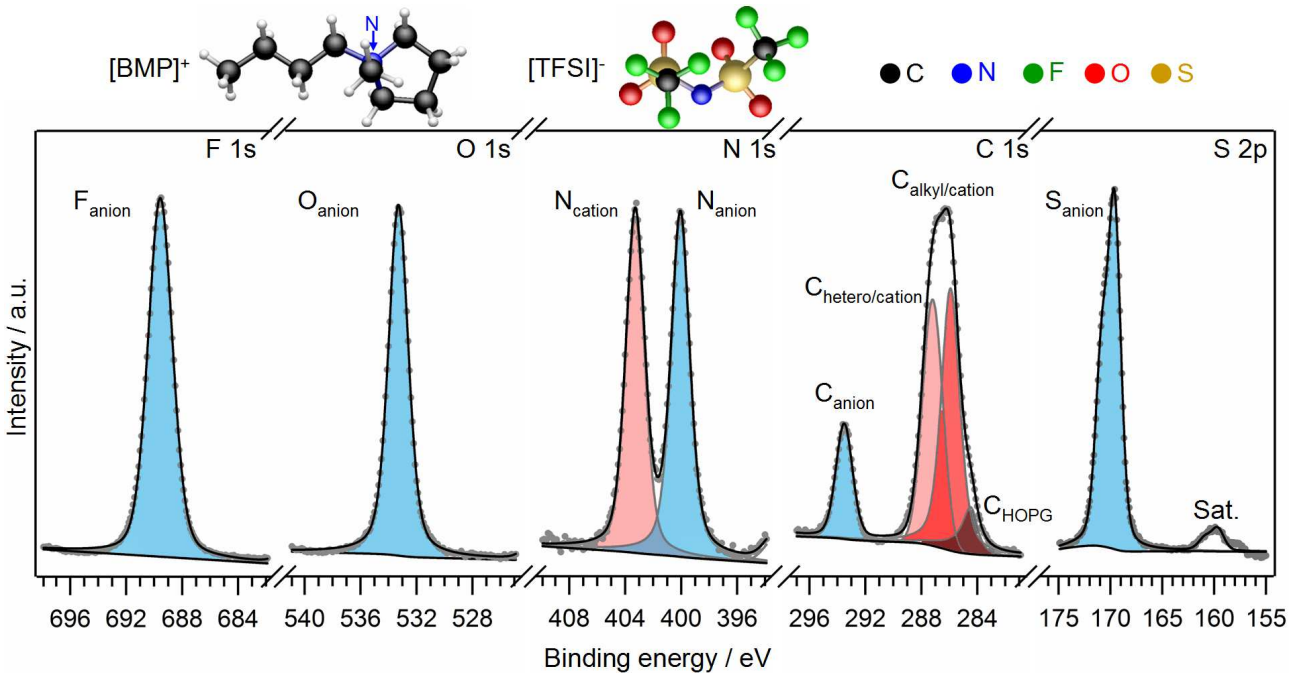

Figure 5. XP F 1s, O 1s, N 1s, C 1s and S 2p core level spectra after vapor deposition of a $[BMP]^+[TFSI]^-$ multilayer on HOPG at r.t.. Molecular representations are inserted on top of the panel.

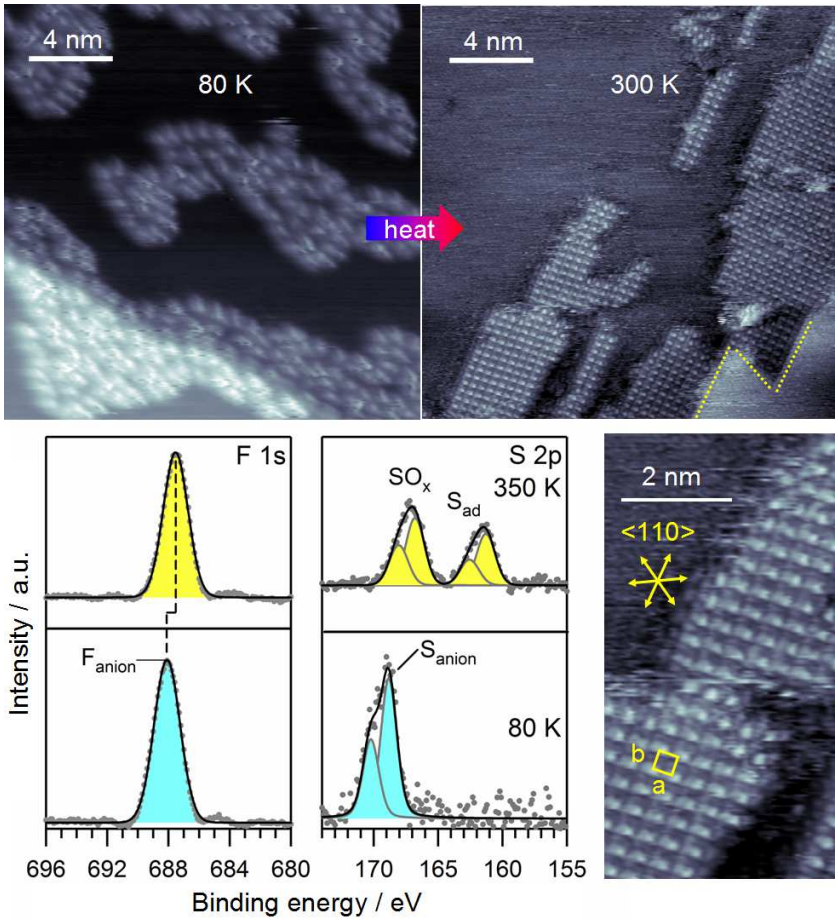

Figure 6. STM images recorded after deposition of an adsorbed monolayer of $[BMP]^+[TFSI]^-$ on Cu(111) at ~ 100 and after heating to 350 K. XP F 1s and S 2p signals of a $[BMP]^+[TFSI]^-$ monolayer at 80 K and after heating to ~ 350 K (bottom left).

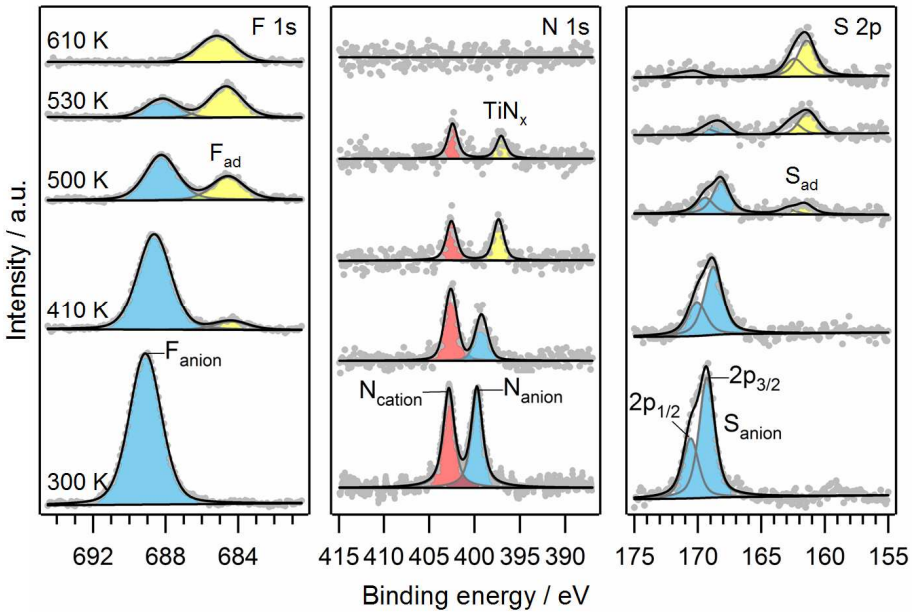

Figure 7. F 1s, N 1s and S 2p core level spectra recorded after adsorption of a $[BMP]^+[TFSI]^-$ monolayer on rutile $TiO_2(110)$ at r.t. and upon subsequent annealing to the temperatures indicated.

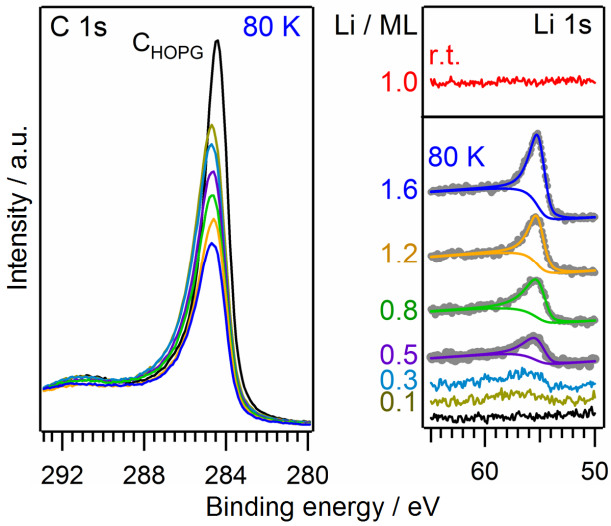

Figure 8. C 1s and Li 1s core level spectra after stepwise vapor deposition of Li on HOPG at 80 K and Li 1s spectrum after vapor deposition of 1 ML of Li on pristine HOPG at r.t. (red solid line).

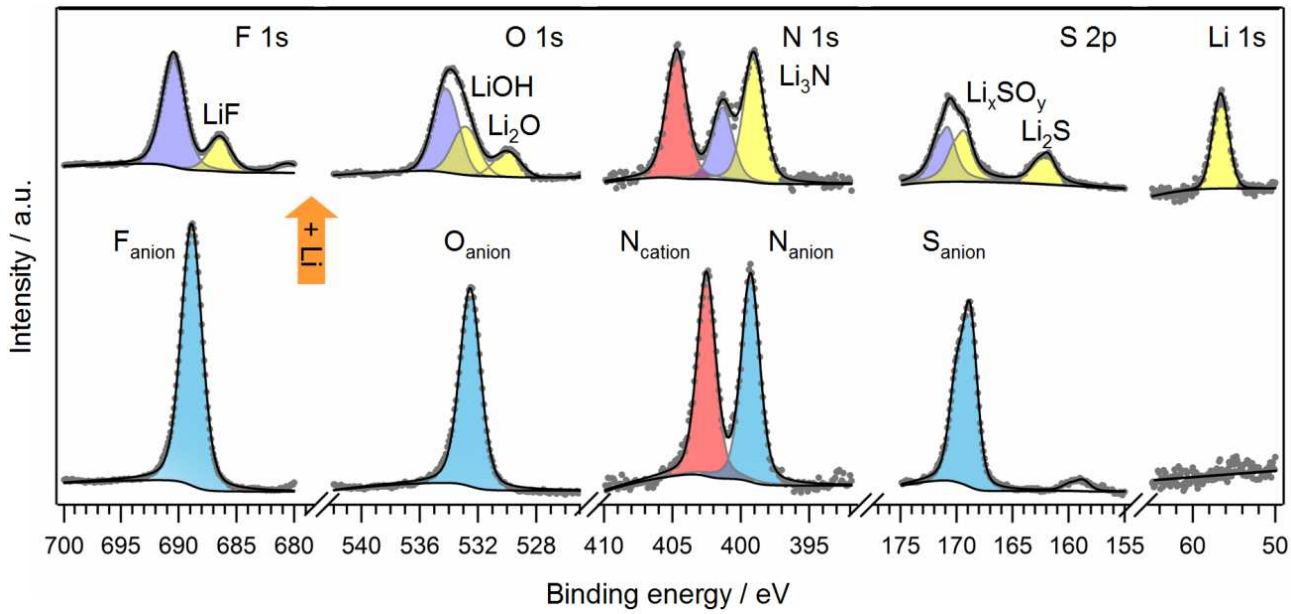

Figure 9. XP F 1s, O 1s, N 1s, S 2p and Li 1s core level spectra of a monolayer of Li-free $[BMP]^+[TFSI]^-$ on graphite(0001) at r.t. (bottom of each panel) and after postdeposition of 1.6 ML of Li (top of each panel).

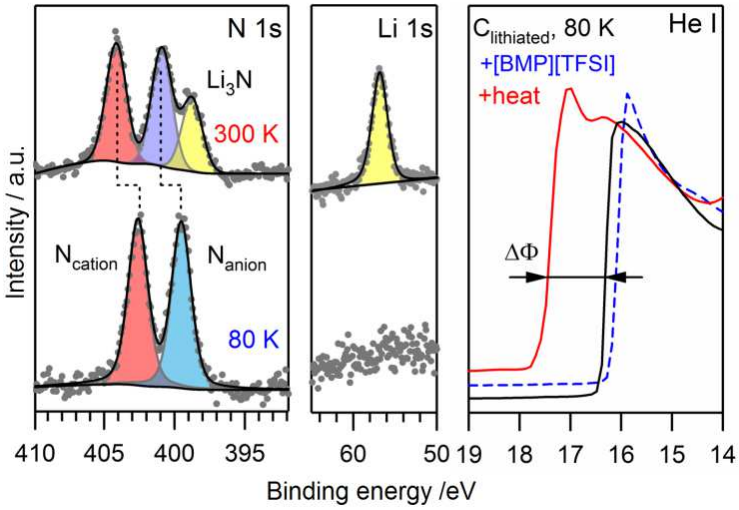

Figure 10. N 1s and Li 1s core level spectra and measurements of the work function Φ after vapor deposition of a $[BMP]^+[TFSI]^-$ monolayer on lithiated HOPG at 80 K (bottom of the panels) and subsequent annealing to r.t (top of the panels).

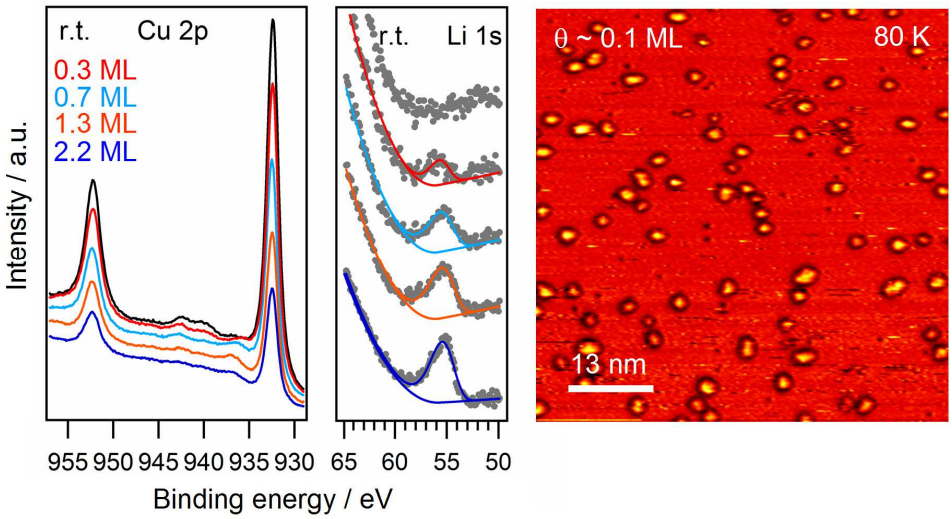

Figure 11. Cu 2p and Li 1s core level spectra after vapo deposition of Li on Cu(111) at r.t. and STM image acquired at 100 K after vapor deposition of a small amount of Li on Cu(111) directly at 80 K.

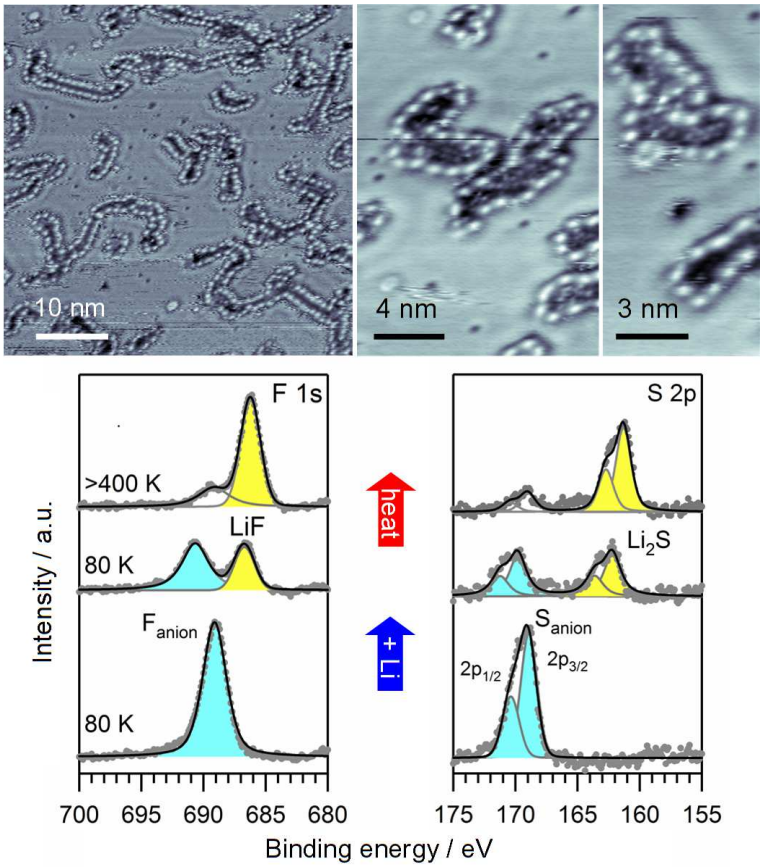

Figure 12. STM images after postdeposition of Li to an adsorbed monolayer of $[BMP]^+[TFSI]^-$ on Cu(111) at 100 K. XP F 1s and S 2p signals before and after postdeposition of Li at 80 K and subsequent heating to > 400 K.

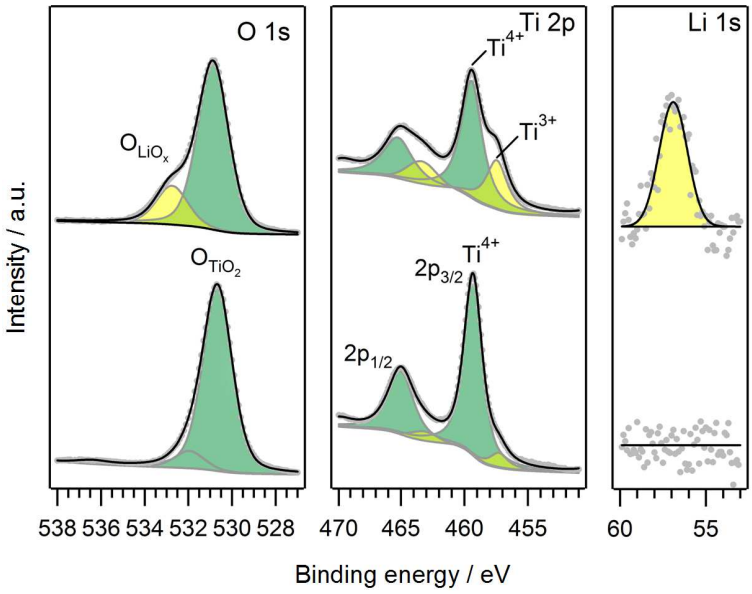

Figure 13. O 1s, Ti 2p and Li 1s core level spectra of pristine TiO_2(110) and upon successive vapor deposition of 1.5 ML of Li at 80 K.

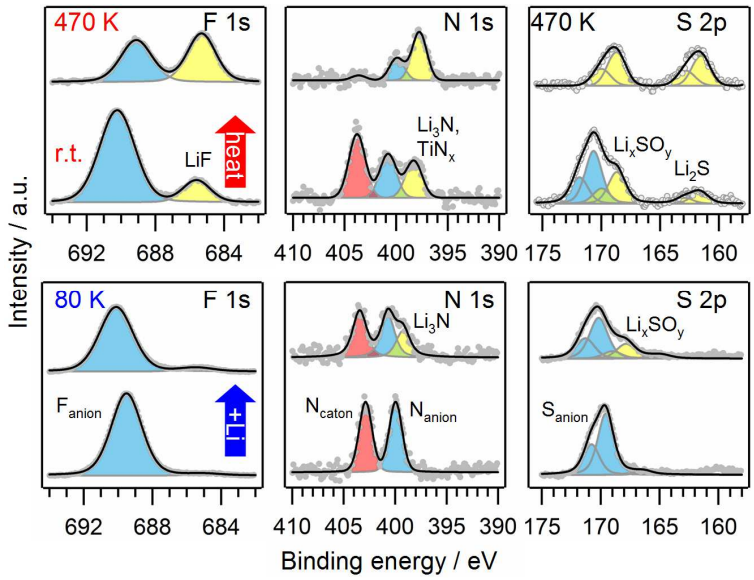

Figure 14. XP F 1s, N 1s and S 2p detail spectra of an adsorbed $[BMP]^+[TFSI]^-$ (sub-)monolayer on TiO_2(110) at 80 K and after postdeposition of Li (panels at the bottom). Mixed $[BMP]^+[TFSI]^-$ adlayer on TiO_2(110) at r.t. and subsequent heating to 470 K (panels on top).